A study of the metal-insulator transition in perovskite-type titanates

ペロブスカイト型チタン酸化物の金属-絶縁体転移の研究

Takuro Katsufuji

勝藤 拓郎

A study of the metal-insulator transition in perovskite-type titanates

Takuro Katsufuji

Contents

Chapter 1

Introduction

Electron-correlation effect and resultant electron localization (a Mott insulator) have long been an important subject of condensed matter physics [1]. $3d$ transition-metal oxides are typical systems, which often become insulating with magnetic ordering due to the strong on-site Coulomb repulsion between the $3d$ electrons. In some cases, a transition between a metal and a Mott insulator is observed by a slight change of some parameters (a Mott transition). A famous example that shows such a transition is V_2O_3 [2], in which a metal-insulator transition at the lowest temperature occurs with application of pressure. In this case, the varied parameter is the bandwidth, which becomes wider with decreased lattice constants by applying pressure.

Recent discovery of the cuprate superconductors has revived the interest on this problem. For the cuprates, parent materials are Mott insulators with Cu $3d^9$ electron configuration, and become metallic with hole doping, showing superconducting transition at low temperatures [3]. In view of the Mott transition, the metal-insulator transition of the cuprate is induced by a change of the band-filling of the conduction band.

A simple theoretical model describing such electron-correlated systems is the Hubbard model, whose Hamiltonian is

$$H = -t \sum_{ij>\sigma} (c^\dagger_{i\sigma} c_{j\sigma} + h.c.) + U \sum_i n_{i\uparrow} n_{i\downarrow},$$

where t is the hopping energy of electrons and U is the on-site Coulomb repulsion energy. In this model, there are two important parameters; one is the strength of electron correlation U/t, and the other is the number of electrons per site n. On the basis of this model, the metal-insulator transition of V_2O_3 is caused by the change of the former parameter, whereas that of the cuprates by the change of the latter parameter [4, 5]. For the systematic studies of the electron-correlated system, therefore, we need a system in which both two parameters, the electron-correlation strength and the electron number, can be controlled independently.

Perovskite-type titanium oxides, $R_{1-x}A_xTiO_3$ (R being a trivalent rare earth, and A a divalent alkaline earth), is a system that satisfies such requirement (Fig. 1.1) [6, 7, 8, 9, 10, 11, 12, 13, 14, 15, 16, 17, 18, 19, 20]. The end compound $RTiO_3$ has $3d^1$ electron configuration in the Ti site, and is a Mott insulator irrespective of the species of R [12]. In other words, this compound is a typical three-dimensional Mott insulator with $n = 1$. The crystal structure of this compound is not completely cubic, but has orthorhombic distortion (the $GdFeO_3$ structure) as shown in Fig. 1.1, and the change of the ionic radius of R induces the change of such distortion. As discussed later in detail, this change of the distortion leads to the change of the bandwidth of the conduction band composed of the Ti $3d$ and oxygen $2p$ orbital. Thus, the change of the species of R corresponds to the change of the electron-correlation strength in this system.

On the other hand, (1) the substitution of the trivalent R ion by the divalent A ion, or (2) the introduction of extra oxygen decreases the number of electrons per Ti site (n) from 1 (nominal hole doping). It is known that with this doping the Mott insulator for $n = 1$ becomes metallic when the nominal hole concentration $\delta = 1 - n$ is ~ 0.08 for $LaTiO_3$, and ~ 0.4 for $YTiO_3$ [10, 13, 14, 15], as shown in Fig. 1.2. Such a metal-insulator (MI) transition with doping is analogous to that of the cuprate superconductors. The metallic state near the phase boundary of the MI transition of these compounds show characteristic behavior of correlated metals, for example, enhanced specific-heat coefficient, Paul paramagnetic susceptibility (Fig. 1.3), and T^2 coefficient of resistivity [13]. Such behavior can be explained theoretically based on the Hubbard Hamiltonian [21].

However, the previous work mainly focused on the R=La system (with a fairly large bandwidth) and the R=Y system (with a relatively small bandwidth), and such studies only on two kinds of rare earth were not sufficient to discuss the dependence of physical properties on their electron-correlation strength, which can be controlled by changing R. Moreover, the previous work has made only qualitative discussion in terms of the two parameters, electron-correlation strength and band filling. We have also little knowledge about what happens at the MI phase boundary of this system, where we expect some characteristic behavior of electron-correlated materials.

The aim of this thesis is to understand the characteristic properties of the electron-correlated system by investigating $R_{1-x}Ca_xTiO_{3-y/2}$ as a prototypical three-dimensional electron-correlated system. Unique points of the present work are as follows: (1) A systematic study with changes of both the correlation strength (a systematic change of R) and the band filling (fine control of Ca concentration and extraoxygen). That provides us with an overall feature of the electronic phase diagram of electron-correlated systems as a function of three parameters, correlation strength, band filling, and temperature (2) A detailed study of the compound near the MI phase boundary. We can know characteristic properties of a "barely metallic" phase from this study. (3) Optical spectroscopy with changes of bandwidth, band filling, and temperature. That allows the discussion of the electronic structures of the electron-correlated system in a more quantitative way than that

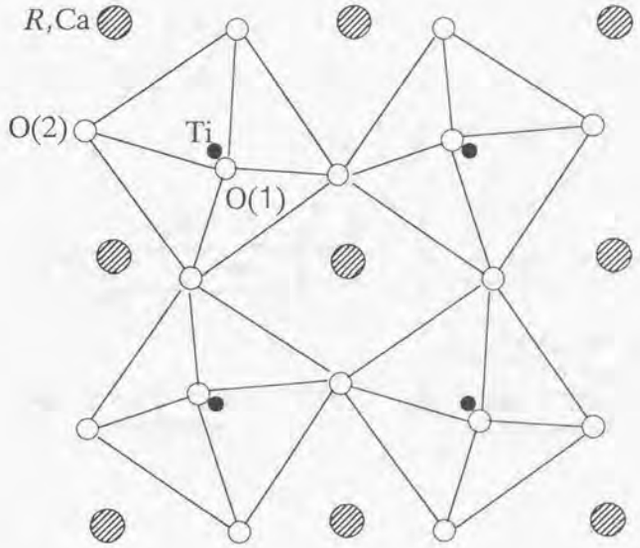

Figure 1.1: Schematic figure of the $GdFeO_3$-type structure.

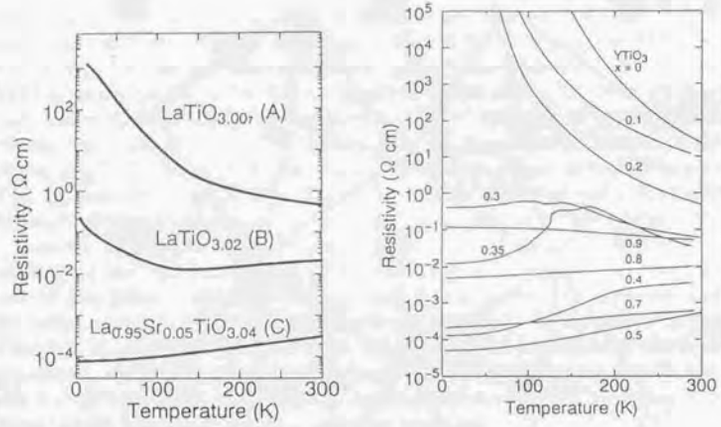

Figure 1.2: Temperature dependence of resistivity for $La_{1-x}Sr_xTiO_{3+y/2}$ (the left side, from Ref. [15]) and $Y_{1-x}Ca_xTiO_{3+y/2}$ (the right side, from Ref. [14]).

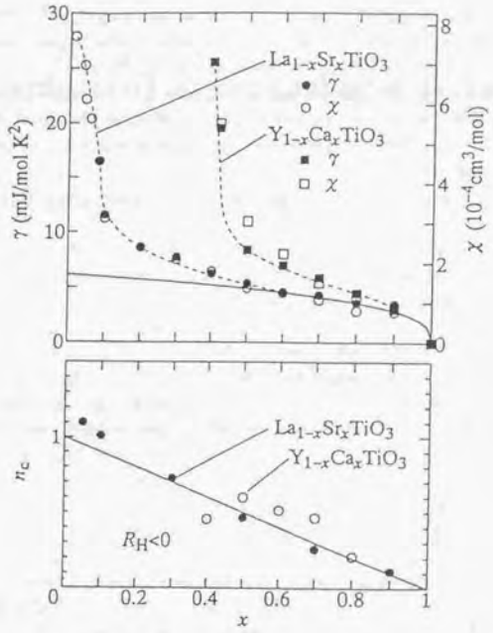

Figure 1.3: The upper panel: the x dependence of electron specific-heat coefficient (γ) and Pauli paramagnetic susceptibility (χ) for $La_{1-x}Sr_xTiO_{3+y/2}$ and $Y_{1-x}Ca_xTiO_{3+y/2}$. The lower panel: x dependence of the effective carrier number obtained from the Hall coefficient measurement for $La_{1-x}Sr_xTiO_{3+y/2}$ and $Y_{1-x}Ca_xTiO_{3+y/2}$. (From Ref. [18])

based on a conventional experimental technique.

The format of this thesis is as follows: Chapter II describes the sample preparation, and transport and magnetic properties of $R_{1-x}Ca_xTiO_{3+y/2}$. On the basis of such results, the electronic and magnetic phase diagram of $R_{1-x}Ca_xTiO_{3+y/2}$ is presented here. In chapter III, optical spectra of $R_{1-x}Ca_xTiO_{3+y/2}$, particularly their bandwidth (W) and hole-concentration ($\delta = 1 - n$) dependence, is presented. We discuss the relation between the electron-correlation strength (U/W) and the Mott-gap magnitude in the end compound, and the relation between U/W and the evolution rate of the in-gap spectra with doping. In chapter IV, optical spectra for the metallic crystals of $R_{1-x}Ca_xTiO_{3+y/2}$ with changing temperature are presented. We discuss such a temperature-dependent spectra on the basis of the extended Drude analysis. In chapter V, phonon Raman spectra of the metallic phase, which couples with the excitation across the Fermi surface, are presented. Chapter VI is devoted to concluding remarks.

Chapter 2

Transport and magnetic properties

2.1 Sample preparation and experiment

All the samples investigated in this study were prepared by the floating zone method similarly to the previous work [15]. Starting materials are R_2O_3 (R=La, Pr, Nd, Sm, and Y), TiO_2, Ti, and $CaTiO_3$. $CaTiO_3$ was synthesized by firing $CaCO_3$ and TiO_2 in air at 1000 C° for 24 h. Stoichiometric amount of sources for $R_{1-x}Ca_xTiO_3$, which had been well dried in advance, were mixed and pressed into rods with $\sim$ 5mm ϕ. To keep the stoichiometry of oxygen, we have omitted a sintering procedure, and directly melted the pressed bar with use of a floating zone furnace equipped with two halogen lamps and ellipsoidal mirrors. Atmosphere in the furnace during the crystal growth was varied to control the oxygen offstoichiometry of the samples (y), which was determined by the thermogravimetric analysis (TGA). The stoichiometric $RTiO_{3.00}$ could be obtained in gas flow of 30 % H_2/Ar, whereas the melting in gas flow of Ar (6N) often results in the excess oxygen ($y/2 = 0.04$ as a typical value). We assume that the ratio of R, Ca, and Ti does not change from the starting ratio. Thus, the nominal hole concentration δ is given by $x + y$.

X-ray powder diffraction was measured and showed that crystal structure of all the samples investigated here is $GdFeO_3$ type. Lattice constants (a,b,and c) are shown in Fig. 2.1. The anisotropy of the lattice constants becomes larger with smaller ionic radius of R and smaller Ca concentration, as shown in Fig. 2.2, where the ratio of a to b is plotted.

Resistivity measurements were carried out by the conventional four-probe technique using indium as an electrode. Magnetization measurement was performed using a SQUID magnetometer.

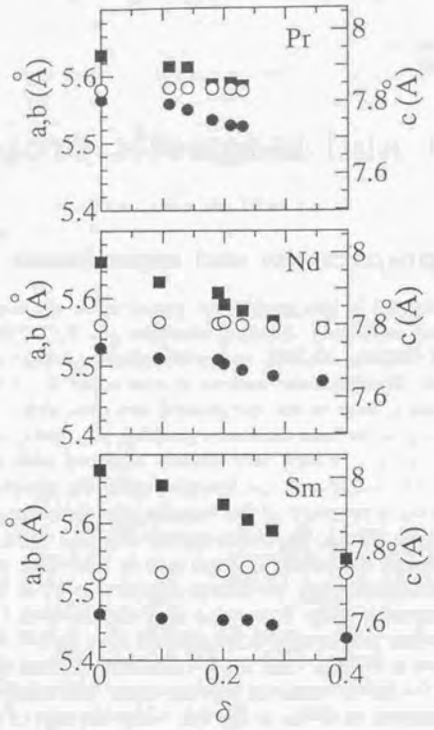

Figure 2.1: Lattice constants of $R_{1-x}Ca_xTiO_{3+y/2}$ for R=Pr, Nd, and Sm against δ. Closed circles and squares represent a and b respectively on the left axis, whereas open circles represent c on the right axis.

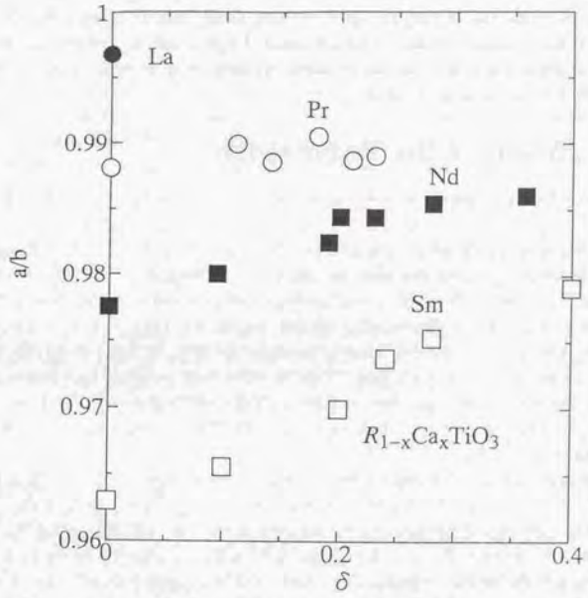

Figure 2.2: Anisotropy of lattice constants (a/b) for various species of R and hole concentrations δ. The value of $LaTiO_3$ is from Ref. [6].

	La	Pr	Nd	Sm	Y
Ti-O(1)-Ti bond angle (degree)	157.5	(152.8)	150.7	146.8	140.3
Ti-O(2)-Ti bond angle (degree)	156.9	(152.3)	150.3	147.0	143.7
W (eV)	2.45	2.33	2.27	2.16	2.04
$\tilde{W}$	1	0.95	0.93	0.88	0.83

Table 2.1: Ti-O-Ti bond angle and bandwidth of the conduction band of RTiO$_3$. The values of bond angle are from Ref. [6] except for PrTiO$_3$, whose bond angles(in parentheses) are obtained by the interpolation of LaTiO$_3$ and NdTiO$_3$ using their tolerance factors. O(1) and O(2) refer to the oxygens at two different sites of the GdFeO$_3$ structure. W is the full-width of the conduction band calculated with tight-binding approximation. $\tilde{W}$ is the ratio of W of each RTiO$_3$ to that of LaTiO$_3$.

2.2 Calculation of the bandwidth

The conduction band of this system is composed of the Ti $3d$ t_{2g} orbital and O $2p$ π orbital, and its bandwidth is governed by the Ti-O-Ti bond angle. These GdFeO$_3$-type titanates have the tilting TiO$_6$ octahedra, which leads to the decrease of the Ti-O-Ti bond angle from 180°. Complete structural parameters were previously determined for RTiO$_3$ by MacLean *et al.* [6], and with use of their data, the one-electron bandwidth of the conduction band for RTiO$_3$ can be calculated by a tight-binding model, where the Hamiltonian matrix based on the Harrison's parameterization [22] taking account of Ti $3d$ t_{2g} and O $2p$ orbital with GdFeO$_3$ lattice distortion are diagonalized. The Ti-O-Ti bond angles and the full-width of the conduction band from the calculation (W) are listed in Table 2.1. $\tilde{W}$ is the ratio of W of each RTiO$_3$ to that of LaTiO$_3$. Among these, the minimal bandwidth of YTiO$_3$ is 83 % of the maximal one of LaTiO$_3$.

Ca doping may also induce a change in the Ti-O-Ti bond angle and resultantly in the bandwidth of the conduction band. Since the Ti-O-Ti bond angle of R_{1-x}Ca$_x$TiO$_{3+y/2}$ with finite value of x has not experimentally been determined so far, we estimated the change of a tolerance factor [1] instead of the bond angle. The tolerance factor of LaTiO$_3$ is 0.95 and that of YTiO$_3$ is 0.89, whose difference is $\sim 6\%$. On the other hand, those of NdTiO$_3$ and Nd$_{0.8}$Ca$_{0.2}$TiO$_3$ are 0.92 and 0.93 respectively, whose difference is only $\sim 1\%$. Thus, as long as properties in the small-x region are discussed, the change of the bond angle with Ca doping would be negligible, and from now on we ignore the change of the bandwidth with Ca doping.

In the spirit of the Hubbard model, the electron-correlation strength is given by U/W,

[1] The tolerance factor of the perovskite structure is given by $t = (r_R + r_O)/[\sqrt{2}(r_{Ti} + r_O)]$, where r_R, r_{Ti}, and r_O are the ionic radii of the rare earth, titanium, and oxygen, respectively, which was tabulated by R. D. Shannon [Acta Cryst. A 32, 751 (1976)]. Concerning the doped sample, we assume that r_R and r_{Ti} are the mean values of R and Ca, and Ti^{4+} and Ti^{3+}, respectively.

where U is the on-site Coulomb repulsion energy. Since the U value can be viewed as constant among the RTiO$_3$ series, $\tilde{W}^{-1}$ is used to represent the electron-correlation strength below.

2.3 Transport properties

Figure 2.3 shows the temperature dependence of the resistivity for R_{1-x}Ca$_x$TiO$_{3+y/2}$ with R=La, Pr, Nd, and Sm, and with various hole concentrations. Results for Y$_{1-x}$Ca$_x$TiO$_3$ have been published in Ref. [14]. For any R, the change of resistivity with hole doping is similar: With increase of hole concentration δ, the temperature dependence of resistivity varies from insulating with thermal activation type to metallic ($d\rho/dT$ is positive). However, there are several R-dependent features. (1) The resistivity for the end compound ($\delta = 0$) increases from R=La to Sm (with decrease of W). (2) The hole concentration that is required to make the system metallic increases from La to Sm. For example, $\delta = 0.08$ is sufficient to make LaTiO$_3$ metallic whereas the sample with $\delta = 0.09$ is still insulating for Nd$_{1-x}$Ca$_x$TiO$_{3+y/2}$.

To discuss the former point more quantitatively, we show an Arrhenius plot of the resistivity for the end compounds RTiO$_3$ in Fig. 2.4. All the data approximately follow the activation-type function $\rho(T) = \rho_0 \exp(\Delta_{act}/k_B T)$, where activation energy Δ_{act} (the slope of the line) decreases from YTiO$_3$ to LaTiO$_3$. We estimate the Δ_{act} value of RTiO$_3$ from the high-temperature part, and plot $2\Delta_{act}$ as a transport gap against the inverse bandwidth $\tilde{W}^{-1}$ in Fig. 2.5. The $2\Delta_{act}$ value decreases linearly with a decrease of $\tilde{W}^{-1}$. The solid line in Fig. 2.5 is the result of least-square fitting of the data with a linear function. This fitting suggests that $2\Delta_{act}$ becomes zero at finite value of $\tilde{W}^{-1}$ (~ 0.95). These experimental results indicate that the relation between the magnitude of the Mott-Hubbard gap (E_g) depends on the electron-correlation strength (U/W) in such a way that $E_g \propto U/W - (U/W)_c$. Here, $(U/W)_c$ is the hypothetical point for the Mott transition with the $n = 1$ ($\delta = 0$) filling. We note that recent calculations of the Hubbard model at infinite dimensions [23, 24] confirmed a metal-insulator transition for $n = 1$ with a finite value of U/W.

The critical R-dependence of transport properties also emerges when the hole doping (δ) into the end compound RTiO$_3$ causes the metal-insulator transition. In Fig. 2.6, insulating and metallic samples are plotted by closed circles and open circles, respectively, in a $\tilde{W}^{-1}$-δ space. Here, we define an insulator as the one whose $d\rho/dT$ is negative over the whole temperature range. It is clear from this figure that the nominal hole concentration that is needed to cause the metal-insulator transition (δ_c) increases with increase of electron-correlation strength $\tilde{W}^{-1}$. The $\tilde{W}^{-1}$ dependence of δ_c appears to be a linear function, as indicated by a solid line. Moreover, the $\tilde{W}^{-1}$ value at which δ_c becomes zero approximately coincides with the one at which $2\Delta_{act}$ becomes zero in Fig. 2.5. This indicates a close interrelation between δ_c and the magnitude of the Mott gap in the end compound. That is

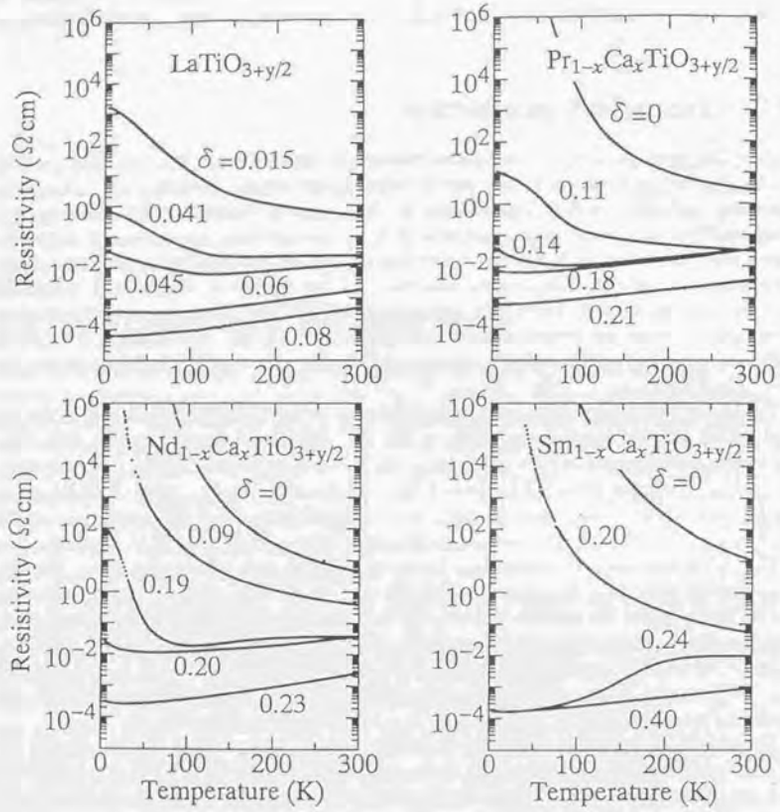

Figure 2.3: Temperature dependence of resistivity in crystals of $R_{1-x}Ca_xTiO_{3+y/2}$ for R=La, Pr, Nd, and Sm with various hole concentrations $\delta = x + y$. The result of R=Y is shown in Ref. [14].

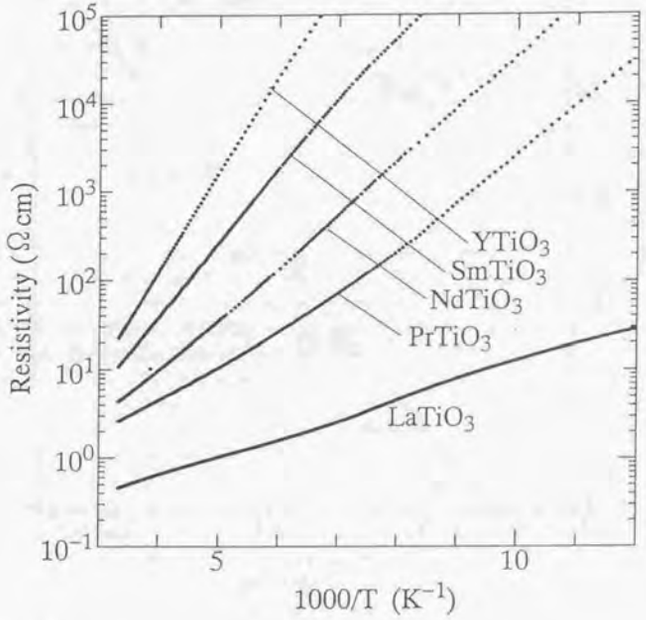

Figure 2.4: Resistivity on a logarithmic scale vs. the inverse of temperature for $RTiO_3$.

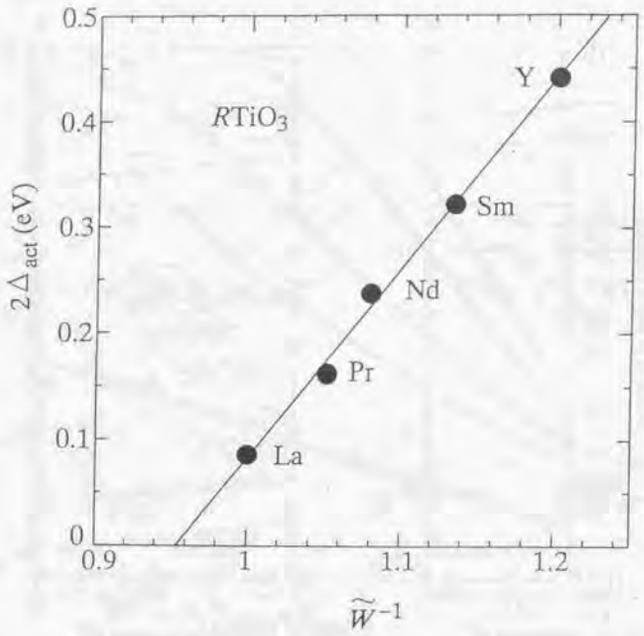

Figure 2.5: $2\Delta_{act}$ vs. $\tilde{W}^{-1}$ for RTiO$_3$. Δ_{act} is the activation energy of resistivity and $\tilde{W}$ is the bandwidth of RTiO$_3$ normalized to that of LaTiO$_3$. The solid line is the result of least square fitting with a linear function.

to say, δ_c increases in proportion with the transport gap in the end Mott insulator. On the basis of a simple three-dimensional Hubbard model that takes account of only the on-site Coulomb interaction, the system should become metallic with non-zero δ. The insulating phase with finite δ in $R_{1-x}Ca_xTiO_{3+y/2}$ is perhaps caused by some combined effect of the electron correlation and others (static disorder or electron-phonon interaction), which is discussed in the latter section.

2.4 Magnetic properties and phase diagrams

The end compounds RTiO$_3$ with relatively large ionic radius for R are known to show antiferromagnetism with slight spin-canting, giving rise to a small spontaneous magnetization [9]. To determine the antiferromagnetic(AF)-ordering temperature T_N of each sample, magnetization measurements were carried out by the following procedure: The sample was at first cooled down to 5K with application of magnetic field of 50000 Oe, then the magnetic field was decreased to 100 Oe, and the magnetization of the sample was measured in a warming run. The temperature dependence of the measured magnetization of RTiO$_3$ is shown in Fig. 2.7, where T_N for each compound is indicated by an arrow. The results for R=La, Pr, Nd are consistent with those previously reported [10, 7, 19]. As far as we know, the AF ordering of SmTiO$_3$ is observed for the first time in the present study. On the other hand, YTiO$_3$ shows ferromagnetic ordering below $T_C \sim 30$ K [14, 9].

In Fig. 2.8 the magnetic-ordering temperatures of RTiO$_3$ are plotted by closed circles together with the results reported by Greedan [9], as a function of $\tilde{W}^{-1}$. In the same figure results for $La_{1-x}Y_xTiO_3$ together with those by Goral *et al.* [25] are also plotted for comparison, where the Néel temperature (T_N) decreases with increase of Y concentration (increase of $\tilde{W}^{-1}$) down to zero, and then a ferromagnetic ordering appears and the Curie temperature (T_C) increases with further increase of Y concentration. The result of RTiO$_3$ with change of the species of R in the present study also follows this trend, when both of them are plotted as a function of $\tilde{W}^{-1}$. However, it should be noted that a simple one-band Hubbard model hardly explains such a rapid decrease of T_N and the appearance of ferromagnetic ordering with an increase in $\tilde{W}^{-1}$. In RTiO$_3$, conduction electrons are accommodated in nearly triply degenerate Ti $3d$ t_{2g} orbitals, and the degenerate (multi-band) Hubbard model seems appropriate to describe the experimental results. Recently, Mizokawa *et al.* [26] investigated the spin structure of RTiO$_3$ by a Hartree-Fock calculation and found that ferromagnetic ordering is favored when taking account of the degeneracy of $3d$ orbitals. However, they claimed that the change of W alone does not explain the change of the spin structure from antiferromagnetic to ferromagnetic ordering, but that a Jahn-Teller distortion is important. In any case, the ferromagnetic ordering is accompanied by the ordering of the degenerated $3d$ orbitals. In fact, such an orbital ordering has recently been confirmed by a polarized neutron-scattering experiment [27]. Moreover, a recent band

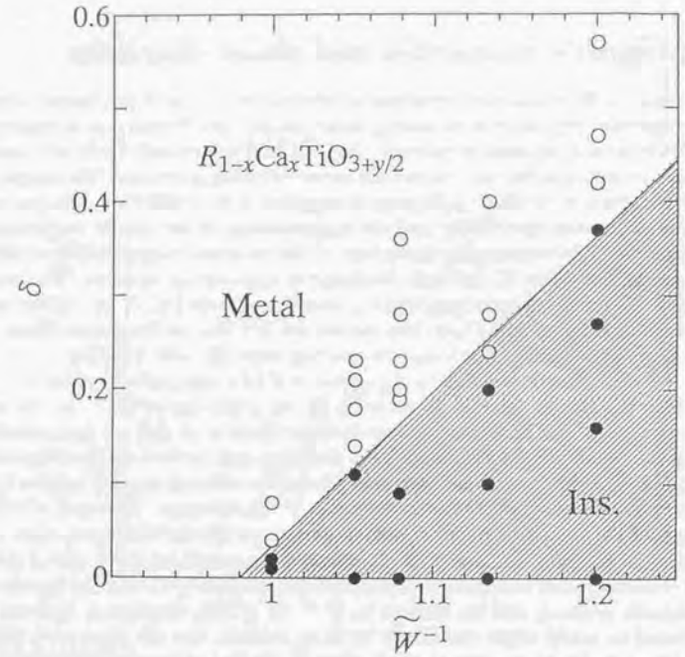

Figure 2.6: Insulating crystals (closed circles) and metallic ones (open circles) are plotted in $\tilde{W}^{-1}$-δ space. For the definition of "metallic" and "insulating" crystals, see text. The solid line is the guide to the eyes, representing a linear relation that separates the space into insulating and metallic regions.

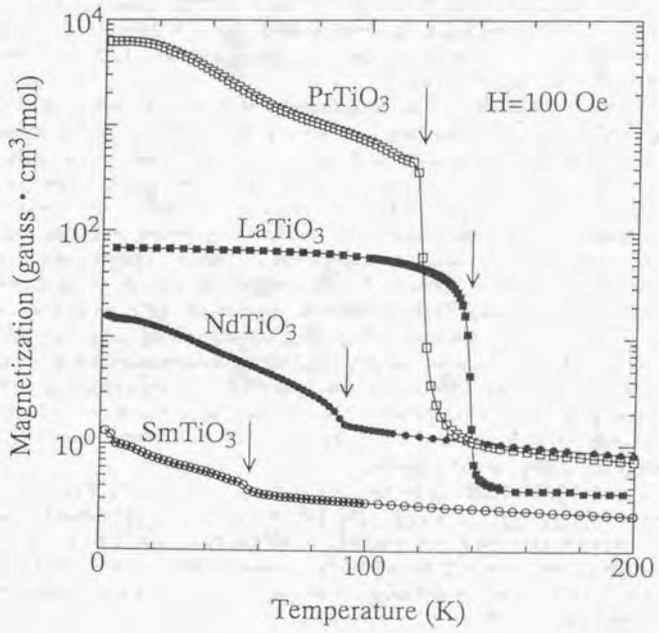

Figure 2.7: Magnetization of RTiO$_3$ at 100 Oe in a warming run, after the cooling the sample under 50000 Oe. Arrows correspond to the antiferromagnetic ordering temperatures.

calculation of $YTiO_3$ by the generalized gradient approximation (GGA) taking account of its $GdFeO_3$ distortion succeeds in reproducing a ferromagnetic spin state with the orbital ordering.

As shown in Fig. 2.7, the magnitude of the magnetization below T_N differs by several orders of magnitude depending on the species of R. We measured the magnetization curves at 5 K for $PrTiO_3$ and $NdTiO_3$ as shown in Fig. 2.9. For $PrTiO_3$ large hysterisis was found with magnetic field whereas almost no hysterisis for $NdTiO_3$. Neutron scattering measurements of these compounds indicate that $PrTiO_3$ [8] and $NdTiO_3$ [20] have qualitatively the same spin configuration both at the Ti site and the rare-earth site below T_N. At present it is not clear why the M-H curve below T_N behaves differently with different species of rare earth. We speculate, however, that such a variety in the magnetism of $RTiO_3$ arises from the $3d$-$4f$ interaction between Ti and R.

We measured the magnetization of $R_{1-x}Ca_xTiO_{3+y/2}$ with finite $\delta(=x+y)$. The results for $Pr_{1-x}Ca_xTiO_{3+y/2}$ and $Sm_{1-x}Ca_xTiO_{3+y/2}$ are exemplified in Fig. 2.10. The magnetization of $Nd_{1-x}Ca_xTiO_3$ was also measured and found to agree with that previously reported [19]. Irrespective of R, T_N decreases and finally disappears with increase of δ for the respective compound. Figure 2.11 is a plot of T_N as a function of δ. Dashed lines correspond to the metal-insulator phase boundary determined by resistivity measurements as described above. The AF phase extends to near the metal-insulator phase boundary for any R, which goes to a higher δ position from R=La to Sm. In other words, the AF phase survives as long as doped holes are localized. Such a correlation between the AF state and the carrier localization is also seen in cuprates such as $La_{2-x}Sr_xCuO_4$ [3] and $R_{2-x}Ce_xCuO_4$ [29], and other transition metal oxides such as $La_{1-x}Sr_xVO_3$ [30]. This phenomenon is qualitatively understood as follows: If doped holes are localized, they will act as impurities with $S = 0$, and such impurities do not effectively destroy the AF ordering as in a diluted spin system. But if a doped hole becomes movable, it will affect many sites with fairly short time scale, and will destroy the long-range AF ordering.

Figure 2.12 shows the electronic phase diagram of the present $R_{1-x}Ca_xTiO_{3+y/2}$ system as a function of U/W, $\delta = x + y$, and T. The T-U/W plane at $\delta = 0$ indicates that T_N decreases with increase of correlation strength U/W for the end compound. The T-δ plane indicates that the T_N decreases with increase of hole concentration δ. The U/W-δ plane at $T = 0$ indicates that both the insulating phase and the antiferromagnetic phase survives up to larger δ with larger U/W.

2.5 Behavior near phase boundaries

As seen in Fig. 2.11, there exists a metallic region where the AF state shows up at low temperature [15]. Figure 2.13 shows resistivity (ρ), the second T-derivative of the resistivity ($d^2\rho/dT^2$), and magnetization (M) at 100 Oe (signaling the AF ordering with slight spin-

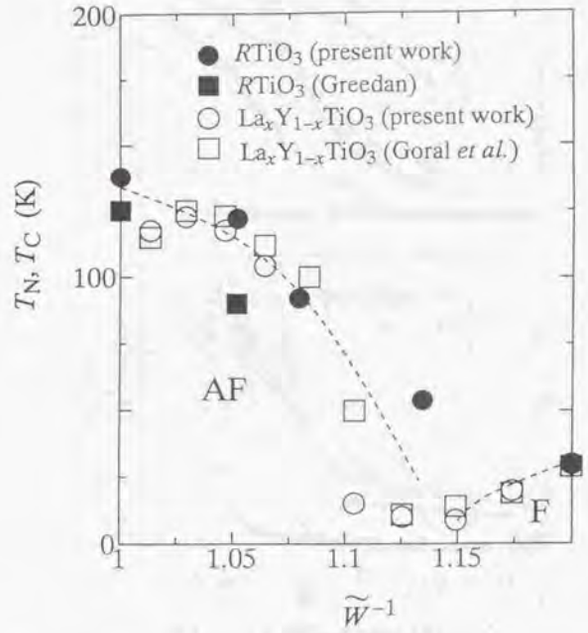

Figure 2.8: Néel (T_N) and Curie (T_C) temperatures of $RTiO_3$ (closed circles) and $La_xY_{1-x}TiO_3$ (open circles) as a function of $\tilde{W}^{-1}$. The data from literature (Ref. [9, 25]) are also shown. The dashed lines are the guide to the eyes.

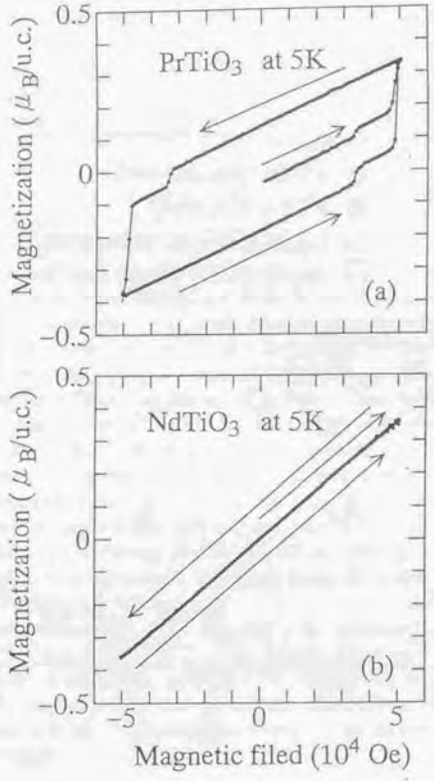

Figure 2.9: Magnetization curves at 5 K for (a) $PrTiO_3$ and (b) $NdTiO_3$.

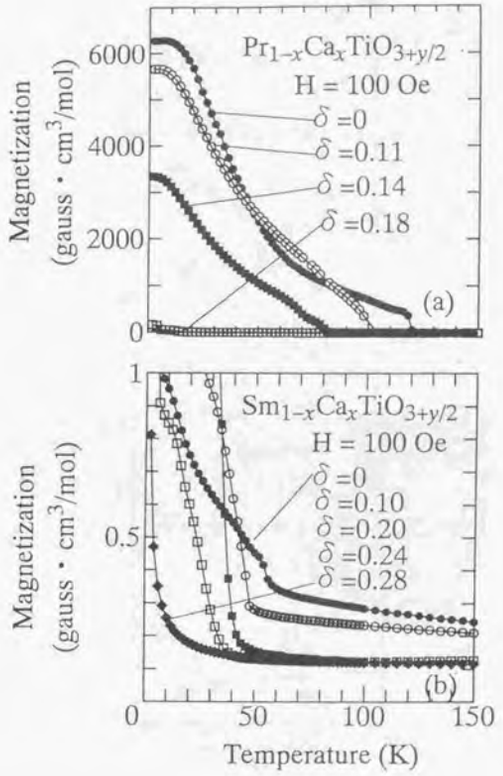

Figure 2.10: Temperature dependence of magnetization for (a) $Pr_{1-x}Ca_xTiO_{3+y/2}$ and (b) $Sm_{1-x}Ca_xTiO_{3+y/2}$. The measurement condition is the same as in Fig. 2.7.

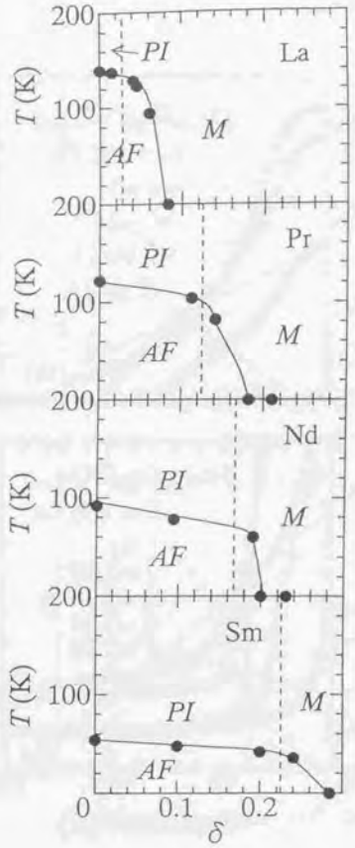

Figure 2.11: Néel temperature for $R_{1-x}Ca_xTiO_{3+y/2}$ as a function of δ. The solid lines are the guide to the eyes. The dashed lines indicate the metal-insulator phase boundary determined from resistivity measurements.

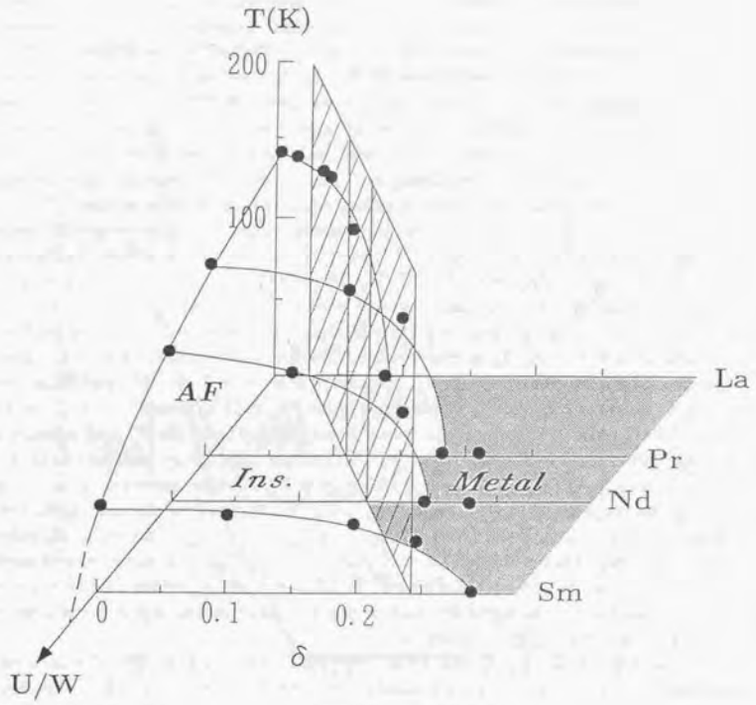

Figure 2.12: The electronic phase diagram of $R_{1-x}Ca_xTiO_{3+y/2}$ in a space of the electron-correlation strength U/W, nominal hole concentration δ, and temperature T.

canting) for $Pr_{1-x}Ca_xTiO_{3+y/2}$ with $\delta = 0.14$, as a typical example in such a region. T_N is $\sim$ 80 K for this sample, and the slope of $\rho(T)$ changes from positive to negative at this temperature. A sharp peak is observed for $d^2\rho/dT^2$ at the same temperature, indicating a steep change of the slope of $\rho(T)$ at T_N. In spite of such a critical change of resistivity with magnetic ordering, the resistivity does not diverge (i.e., the conductivity does not become zero) but remains finite at the lowest temperature (2 K) of the present measurement, as shown in the inset of Fig. 2.13 where conductivity is plotted as a function of T. This indicates that the phase below 80 K is an AF *metallic* phase. Thus, we may call this as the transition from the high-temperature-metal (HTM) to the low-temperature-antiferomagnetic-metal(LTAFM). Such an AF metal has been observed for V_2O_3 with slight V vacancy [31], where a spin density wave with an incommensurate wave vector was observed by neutron diffraction measurement [32]. It would be interesting to investigate whether such an incommensurate spin ordering also exists in these titanates.

The crystals near the border between the metallic phase and paramagentic insulating (PI) phase also show a novel behavior. Figure 2.14 shows the temperature dependence of ρ for $Sm_{1-x}Ca_xTiO_{3+y/2}$ with $\delta = 0.24$. The ρ value at room temperature is $\sim$ 10 mΩcm, and around 200 K it sharply decreases with decrease of temperature down to $\sim$ 0.2 mΩcm. Note that the temperature for the resistivity anomaly does not correspond to that of magnetic ordering, since T_N is much lower than this temperature. A similar resistivity change has also been observed for $Y_{1-x}Ca_xTiO_3$ with $x \sim 0.40$ [16], and these can be regarded as a transition from a high-temperature PI (HTPI) phase to low-temperature metallic (LTM) phase. Therefore, the phase boundary between the PI and metallic state shown by dashed lines in Fig. 2.11 and Fig. 2.12 is not completely parallel to the T-axis, but is slightly inclined (going to larger δ with higher T). Such an electronic phase diagram is quite similar to those of V_2O_3 [2] and $NiS_{2-x}Se_x$ [33, 34], though the abscissa is different for these systems; namely, the band filling for $R_{1-x}Ca_xTiO_{3+y/2}$ and the bandwidth for V_2O_3 or $NiS_{2-x}Se_x$. Recent numerical calculations [21, 35] based on the Hubbard model in infinite dimensions have reproduced the HTPI-LTM transition, which can be interpreted as the disappearance of the coherent peak in the density of states, which is responsible for the metallic conduction, with increase of T.

In the metallic phase of $La_{1-x}Sr_xTiO_3$, the resistivity ρ follows T^2 relation from the lowest temperature to fairly high temperature ($\sim$ 300 K) [13]. Such a T^2 dependence of the resistivity ρ is also observed for the metallic phases of other R systems. However, a deviation from this T^2 relation is observed in the vicinity of the metal-insulator phase boundary. In Fig. 2.15 we plot ρ as a function of T^2. Here, the residual resistivity (ρ_0) is subtracted and the values of $\rho - \rho_0$ are normalized for the respective compounds so that the slope appears the same. For $Pr_{1-x}Ca_xTiO_{3+y/2}$, the ρ value for $\delta = 0.21$ shows the T^2 relation down to the lowest temperature, whereas as δ decreases ρ begins to deviate from the T^2 relation at low temperatures. This deviation is apparently related to the HTM-LTAFM transition as described above. For $\delta = 0.14$ T_N is 80 K (approximately corresponding

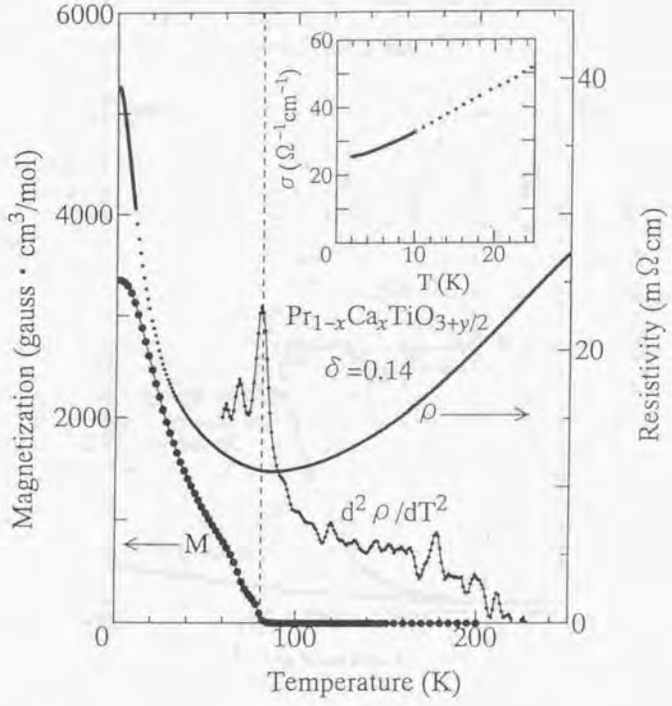

Figure 2.13: Magnetization (M) at 100 Oe, resistivity (ρ), and second T-derivative of ρ as a function of temperature (T) for $Pr_{1-x}Ca_xTiO_{3+y/2}$ with $\delta = 0.14$. The inset is a plot of the conductivity ($= 1/\rho$) against T.

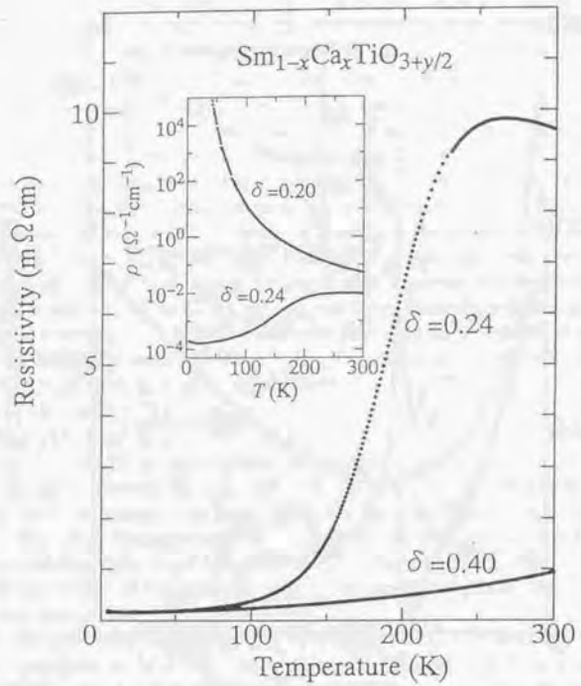

Figure 2.14: Temperature (T) dependence of resistivity (ρ) for $Sm_{1-x}Ca_xTiO_{3+y/2}$ with $\delta = 0.24$ and 0.40. The inset shows the T dependence of ρ for $Sm_{1-x}Ca_xTiO_{3+y/2}$ with $\delta = 0.20$ and 0.24 on a logarithmic scale.

to the temperature for the minimum resistivity) but the deviation from T^2 relation is observable up to higher temperature $\sim 140K$. This implies that strong antiferromagnetic fluctuation persists well above T_N in the doped system, which gives rise to additional carrier scattering process other than the normal one contributing the T^2 dependence. On the other hand, the deviation from the T^2 relation is observed for $Sm_{1-x}Ca_xTiO_{3+y/2}$ (and also $Y_{1-x}Ca_xTiO_{3+y/2}$) at higher temperatures, which would be related to the HTPI-LTM transition. For these smaller-W systems, the temperature range where ρ follows the T^2 relation is suppressed to lower temperature as the system approaches the MI transition.

2.6 Summary

We have investigated transport and magnetic properties of $R_{1-x}Ca_xTiO_{3+y/2}$ whose bandwidth (or strength of electron correlation) and band filling can both be controlled by the change of the (R, Ca) composition. The charge-gap magnitude (E_g) of the end compounds $RTiO_3$, as well as the hole concentration required to make the sample metallic (δ_c), change with the correlation strength in a way that $\propto U/W - (U/W)_c$.

The Néel temperature (T_N) in $RTiO_3$ decreases from La to Sm (with decreasing bandwidth W), and $YTiO_3$ becomes a ferromagnet at low temperature. Such a decrease of T_N and appearance of the ferromagnetism should be attributed to the degeneracy of Ti $3d$ t_{2g} orbital as well as the orbital ordering. T_N also decreases with hole doping, but remains finite as long as the compound remains insulating.

The $R_{1-x}Ca_xTiO_{3+y/2}$ crystals near the MI phase boundary show characteristic behavior. One is the transition from a high-temperature-metallic to a low-temperature-antiferromagnetic phase. Resistivity shows an up-turn at the transition temperature but its value remains finite at the lowest temperature (2 K in this experiment), indicating the existence of the antiferromagnetic metallic state. The other is the transition from a high-temperature-paramagnetic-insulating to a low-temperature-metallic phase. In both cases, a deviation from a T^2 dependence is observed for the resistivity in the metallic phases near the phase boundary.

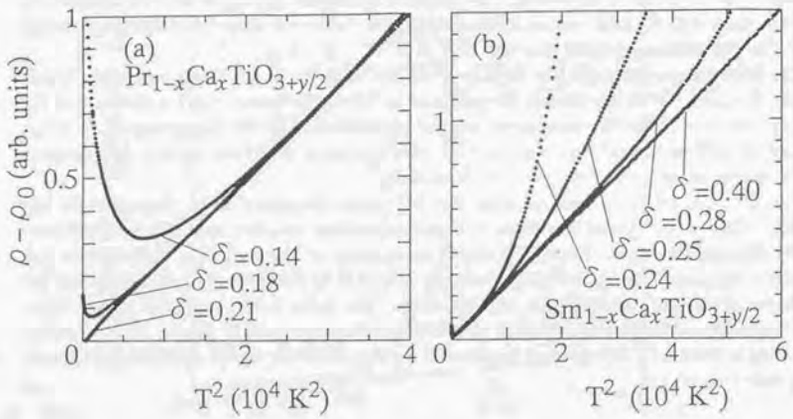

Figure 2.15: $\rho - \rho_0$ vs. T^2 for (a) $Pr_{1-x}Ca_xTiO_{3+y/2}$ and (b) $Sm_{1-x}Ca_xTiO_{3+y/2}$ with various δ. ρ_0 is the residual resistivity and the $\rho - \rho_0$ values are normalized so that the slope becomes the same for all the data.

Chapter 3

Optical spectra: bandwidth and band-filling dependence

3.1 Optical spectroscopy

Reflectivity measurement of solids has been a basic technique to investigate their electronic structures. Reflectivity is determined by a complex dielectric function of crystals, which reflects the excited states of electrons. In particular, this measurement had been used for measuring the electronic structures of insulators and semiconductors.

Since the discovery of the high T_c cuprate superconductors, however, reflectivity measurement has also been applied to investigate metallic states and metal-insulator transitions. For example, reflectivity measurements of the cuprates have clarified that a charge gap caused by electron correlation is present in the end compound, which collapses and the "in-gap state" evolves with hole doping [36, 37, 38]. Furthermore, reflectivity measurements with changing temperature have revealed characteristic properties of cuprate superconductors i.e., opening of the superconducting gap below T_c [39] as well as a normal-state gap above T_c [40, 41].

In this section and the next section, we describe reflectivity measurements of the perovskite-type titanates. In this chapter, bandwidth (W) and band-filling dependence of the optical spectrum of $R_{1-x}Ca_xTiO_{3+y/2}$ is presented and discussed. Temperature dependence of the optical spectra is presented in the next chapter.

3.2 Experiment

We measured reflectivity from 0.01 eV to 40 eV. The way of measuring reflectivity at certain energy ranges is shown in Table. 3.1.

To obtain the absolute value of reflectivity, we measured the intensity of the incident

Energy (eV)	Monochromator	Detector	Light source
0.01-0.08 (Far Infrared)	Fourier-transfer type	Si bolometer	Glober lamp
0.06-0.8 (Mid Infrared)	Fourier-transfer type	HgCdTe	Glober lamp
0.6-1.5 (Near Infrared)	grating type	InAs	halogen lamp
1.2-3 (Visible)	grating type	Si	halogen lamp
2.4-6 (Ultraviolet)	grating type	GaP	Xe lamp
4-40 (Vacuum Ultraviolet)	Seya-Namioka type	photomultiplier	synchrotron radiation

Table 3.1: The way of measuring reflectivity at specific photon-energy ranges in the present experiment.

light by setting a reference mirror (a flat glass on which Au is evaporated) at the sample position below 1.5 eV, where reflectivity of Au is more than 99 % . Above 1.5 eV, we did not use a reference mirror but directly detected the incident light by changing the light pass. We also used a microscope spectrometer in the mid-infrared region (0.05–0.8 eV). This spectrometer can focus the incident light on the clean part of the sample surface, and can avoid the scattering of the light by the rough surface. Thus, the absolute value of reflectivity obtained by this spectrometer is more reliable than that by the conventional method.

Temperature dependence of reflectivity was measured by setting the sample in a He cryostat, in which the sample can be replaced mechanically with the reference mirror.

3.3 Kramers-Kronig transformation

Reflectivity is given by the following equation,

$$R(\omega) = \left| \frac{\sqrt{\tilde{\epsilon}(\omega)} - 1}{\sqrt{\tilde{\epsilon}(\omega)} + 1} \right|^2, \tag{3.1}$$

where $R(\omega)$ is reflectivity and $\epsilon(\omega)$ is complex dielectric function. Since $\epsilon(\omega)$ has the real and imaginary part, they cannot be obtained directly from reflectivity. However, the real and imaginary part of $\epsilon(\omega)$ are not independent but correlated with each other by a Kramers-Kronig relation. By using such a relation, we can obtain both the real and imaginary part of the dielectric function from the experimentally obtained reflectivity.

In practice, we first obtain the phase shift of electric vector of light upon refection $[\theta(\omega)]$, which is given by the reflectivity with the following Kramers-Kronig relation,

$$\theta(\omega) = -\frac{\omega}{2\pi} P \int_0^\infty \frac{\ln R(s)}{s^2 - \omega^2} ds. \tag{3.2}$$

This equation includes the ω integral from zero to infinity, and for the outside of the frequency regin where reflectivity was measured experimentally, we made the constant

extrapolation in the lower-frequency region and $R = \omega^{-1/4}$ extrapolation in the higher-frequency region.

The reflectivity and the phase shift are connected with the complex dielectric function as follows;

$$\sqrt{R(\omega)} \exp(i\theta) = \frac{\sqrt{\tilde{\epsilon}(\omega)} - 1}{\sqrt{\tilde{\epsilon}(\omega)} + 1}. \tag{3.3}$$

Therefore, we can obtain both the real and imaginary part of the dielectric function from the measured reflectivity and the phase shift obtained from Eq. (3.2).

We also obtained the optical conductivity $\sigma(\omega)$, which relates to the imaginary part of the dielectric function in the following way;

$$\sigma(\omega) = \frac{\omega \epsilon_2(\omega)}{4\pi}. \tag{3.4}$$

The zero-frequency limit of $\sigma(\omega)$ should coincide with the dc conductivity (reciprocal resistivity), and this coincidence can be a possible check of the reliability of the experimental data.

Typical reflectivity spectra and corresponding optical conductivity spectra are shown in Fig. 3.1. From now on in this chapter, we present only optical conductivity spectra.

3.4 Optical spectra for $RTiO_3$

Figure 3.2 shows the optical conductivity spectrum of $NdTiO_3$ as a typical $n = 1$ Mott insulator, together with that of $CaTiO_3$ as a typical $n = 0$ band insulator. In the spectrum of $NdTiO_3$ (the solid curve), two structures at 1.5 eV and 5 eV are prominent. In the spectrum of $CaTiO_3$ (the dashed curve), on the other hand, there is no structure corresponding to the 1.5 eV peak of the $NdTiO_3$ spectrum, but the shoulder at 4 eV is likely to correspond to the 5 eV peak of the $NdTiO_3$. Therefore, the 5 eV peaks of the $NdTiO_3$ spectrum and the 4 eV shoulder of the $CaTiO_3$ spectrum can be assigned to the electronic excitation from the occupied oxygen $2p$ level to the unoccupied Ti $3d$ level (upper Hubbard band for $NdTiO_3$), and the 1.5 eV peaks of the $NdTiO_3$ spectrum, which is absent in the $CaTiO_3$ spectrum , can be assigned to the electronic excitation from the occupied (lower Hubbard band) to the unoccupied (upper Hubbard band) Ti $3d$ level, as illustrated in the figure.

The R dependence of the the Mott-gap excitation spectrum (from lower to upper Hubbard band) is shown in Fig. 3.3. The bandwidth of each $R TiO_3$ normalized to that of $LaTiO_3$ ($\tilde{W} = W_R/W_{La}$) is shown in the figure. The structure of the spectrum moves to

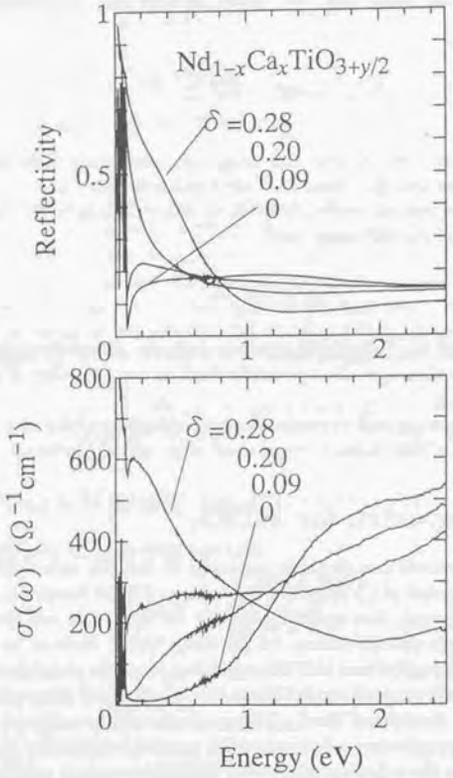

Figure 3.1: Comparison of reflectivity (upper panel) and optical conductivity $[\sigma(\omega)]$ (lower panel) derived from the Kramers-Kronig transformation of the reflectivity, for $Nd_{1-x}Ca_xTiO_{3+y/2}$.

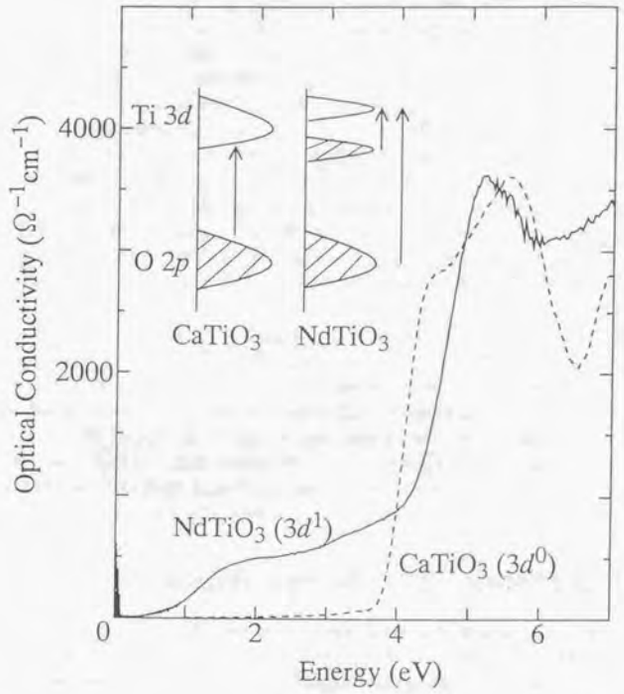

Figure 3.2: Optical conductivity spectra for $NdTiO_3$ ($3d^1$, shown by the solid line) and $CaTiO_3$ ($3d^0$, shown by the dashed line). Schematic pictures of the electronic structures and excitations for both compounds are also shown.
[p]

lower energy with decrease of $\tilde{W}$ (from Y to La). In the study of the Mott-gap structure for V_2O_3 [42], the energy gap 2Δ was determined by fitting the spectra to the form $\sigma = \sigma_0(E - 2\Delta)^{3/2}$. However, such $E^{3/2}$ dependence was not clearly observed in the spectra for the titanates. Thus, we estimated an energy gap 2Δ by extrapolating a steeply increasing part of $\sigma(\omega)$ to zero (dashed lines). The residual spectral weight inside the gap may be assigned to the remnant due to very slight deviation of δ from zero.

Figure 3.4 shows the $\tilde{W}^{-1}$ dependence of 2Δ normalized to W ($2\Delta/W$), together with the activation energy normalized to W ($2\Delta_{\rm act}/W$) determined by resistivity measurements of RTiO$_3$ [$\rho(T) = \rho_0 \exp(\Delta_{\rm act}/k_BT)$]. Here, $\tilde{W}^{-1}$ of the x axis corresponds to the strength of the electron correlation. 2Δ and $2\Delta_{\rm act}$ have nearly the same dependence on $\tilde{W}^{-1}$, i.e., linearly decreases with decrease of $\tilde{W}^{-1}$. We note that similar $\tilde{W}^{-1}$-dependence is observed for V_2O_3 [42]. Extrapolation of the data points of $2\Delta_{\rm act}/W$ by the linear function (a solid line) crosses the $2\Delta = 0$ line (the x axis) at the finite value of $\tilde{W}$ (~ 0.97). It seems reasonable to consider that this value corresponds to the critical value of the bandwidth-control Mott transition [$(U/W)_c$] at which the charge gap closes and the system becomes metallic for $n = 1$.

Recent calculations of the Hubbard model at infinite dimensions [23, 24] confirmed a metal-insulator transition for $n = 1$ with a finite value of U/W, and quantitatively explained the U/W dependence of the magnitude of the Mott gap in V_2O_3, i.e., $2\Delta \propto (U/W) - (U/W)_c$ [42]. It is notable that 2Δ is approximately two times larger than $2\Delta_{\rm act}$. Such deviation may arise from the overestimation 2Δ by the linear extrapolation of the spectra. However, the deviation between the two values ($2\Delta > 2\Delta_{\rm act}$) was also found in V_2O_3 [42], and that has been attributed to the pinning of chemical potential at a weak impurity level, which is not clear in the optical conductivity spectra.

3.5 Optical spectra with hole doping

Figure 3.5 shows $\sigma(\omega)$ spectra for several species of R and various Ca concentrations. Here, δ ($= 1 - n$) stands for the nominal number of holes per Ti site. We show the bandwidth of each RTiO$_3$ normalized to that of LaTiO$_3$ ($\tilde{W} = W_R/W_{\rm La}$) in the figure.

In the case of R=Nd (Nd$_{1-x}$Ca$_x$TiO$_3$), for example, $\sigma(\omega)$ at $\delta = 0$ ($n = 1$) shows negligible spectral weight below 0.8 eV but steeply increases above 0.8 eV, corresponding to the Mott-gap excitation as discussed in the last section. Such a spectrum arising from the Mott-gap excitation is reduced in its intensity with increase of δ, while that inside the gap increases. This in-gap spectrum is pinned to zero conductivity at $\omega \sim 0$ when δ is small (for example, $\delta = 0.09$ for R=Nd), corresponding to the insulating behavior of this crystal in resistivity. The conductivity at $\omega \sim 0$ becomes non-zero when the system becomes metallic ($\delta = 0.18$ for R=Nd), and changes into a Drude-like spectrum (where conductivity decreases with increase of ω) with further increase of δ. We note that such

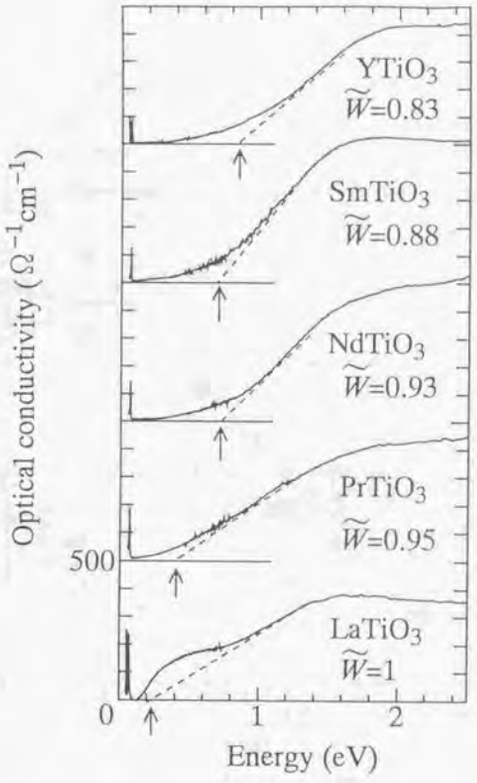

Figure 3.3: Optical conductivity spectra of the compound for $n = 1$ (RTiO$_3$). The bandwidth of each RTiO$_3$ normalized to that of LaTiO$_3$ ($\tilde{W} = W_R/W_{\rm La}$) is also shown in the figure. Dashed lines are the extrapolation of the steeply increasing part of the spectra, and arrows show the intersection of such extrapolated lines and the x axis, representing the energy gap of RTiO$_3$.

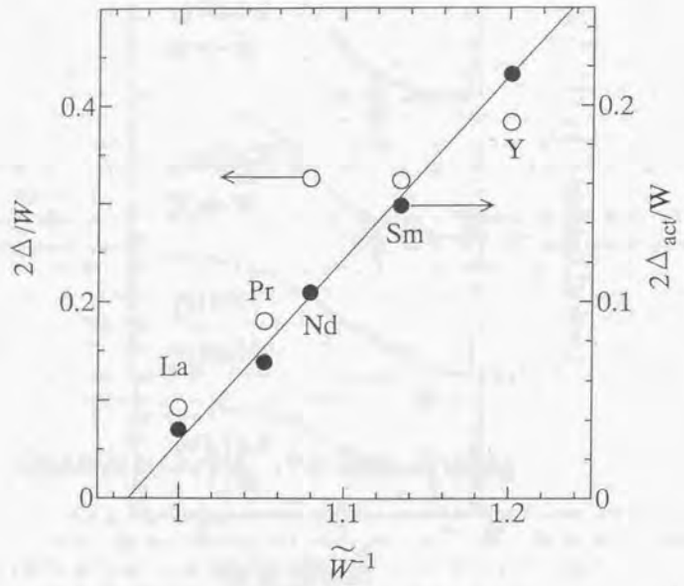

Figure 3.4: $\tilde{W}^{-1}$ dependence of 2Δ (an energy gap obtained by optical conductivity spectra) and $2\Delta_{\rm act}$ (two times activation energy obtained by the temperature dependence of resistivity) normalized to the bandwidth (W). The solid line is the result of least-square fitting of the data of $2\Delta_{\rm act}/W$ to the linear function.

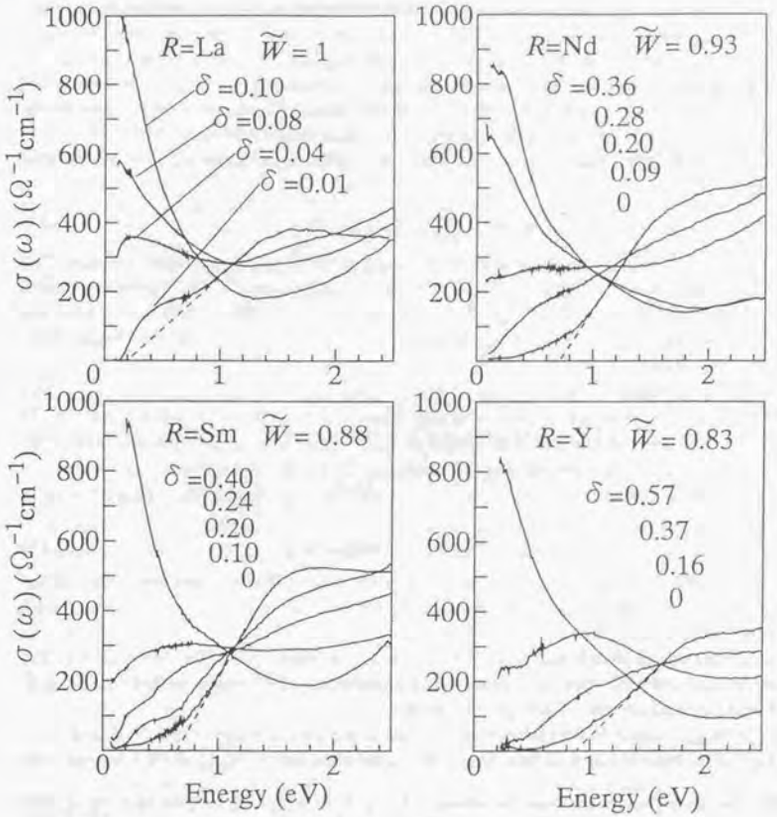

Figure 3.5: Optical conductivity spectra for $R_{1-x}Ca_xTiO_3$ with R=La, Nd, Sm, and Y. δ is nominal hole concentration, i.e., $\delta = 1 - n$ where n is the number of d electrons per Ti site. $\tilde{W} = W_R/W_{\rm La}$ is the one-electron bandwidth of each $RTiO_3$ normalized to that of $LaTiO_3$. Dashed straight lines indicate the energy gap for $\delta = 0$.

a change of the spectrum with doping (a change of band filling) is similar to that of the cuprate, and would be a characteristic behavior for doped Mott insulators.

$\sigma(\omega)$ changes with increase of δ in a similar way irrespective of the species of R as shown in Fig. 3.5. However, it is remarkable that the evolution rate of the in-gap spectrum with δ depends on the species of R. For example, 10 % hole-doping is sufficient for R=La to evolve the Drude-like spectrum with large spectral weight, whereas only the in-gap spectrum with small spectral weight is observed for R=Sm with the same hole concentration. This means that the evolution rate of the in-gap spectrum decreases with decrease of $\tilde{W}$.

To make quantitative discussion of this point, we define the effective number of electrons ($N_{\rm eff}$) as

$$N_{\rm eff}(\omega) = \frac{2m_0}{\pi e^2 N}\int_0^{\omega}\sigma(\omega')d\omega', \tag{3.5}$$

where m_0 is the free electron mass and N the number of Ti atoms per unit volume. This value corresponds to the number of electrons that contributes to the excitation below ω. In the simple Drude model, $N_{\rm eff}$ of the Drude peak (the Drude weight) is identical to $(n_e/N)/(m^*/m_0)$, where n_e and m_0 is the concentration and the effective mass of the conduction carrriers.

We found that $N_{\rm eff}(\omega)$ of the spectra is nearly independent of δ with $\omega = 2.5$ eV, which includes both spectral weights for the in-gap state and for the Mott-gap excitation. In other words, the sum of the spectral weight of these two parts is nearly conserved under variation of δ, but the spectral weight is transferred from the Mott-gap-excitation part to the in-gap part across the isosbetic point ($\sim$ 1.1 eV for $Nd_{1-x}Ca_xTiO_3$). Thus, the value defined as

$$N_{\rm ingap} = N_{\rm eff}(\omega_c)_{\delta} - N_{\rm eff}(\omega_c)_{\delta=0}, \tag{3.6}$$

where ω_c stands for the isosbetic point, is the spectral weight of the in-gap state transferred from the higher-energy region with doping. This value should correspond to the Drude weight for metallic samples.

We adopted ω_c (isosbetic point) of 1.0, 1.1, 1.1, 1.1, and 1.5 eV for R = La, Pr, Nd, Sm, and Y, respectively. Such an increase of the isosbetic point energy with decrease of $\tilde{W}$ reflects the increase of the energy gap 2Δ with $\delta = 0$.

We plot $N_{\rm ingap}$, which is normalized to N_0 that is the Drude weight for $U = 0$ and $\delta = 0$ ($n = 1$), [1] as a function of δ in Fig. 3.6. The linear increase of $N_{\rm ingap}$ with δ is similar to

[1] This value was estimated as follows: We obtained $N_{\rm ingap}$ of $La_{1-x}Sr_xTiO_3$ over the whole filling range from the $\sigma(\omega)$ spectra reported in Ref. [11], and found that $N_{\rm ingap}$ for $x > 0.5$ (i.e., $n < 0.5$) linearly increases with n (not $\delta = 1-n$). Such a relation for the low band filling is in accordance with the result of numerical studies (Ref. [44]); namely $N_{\rm ingap}$ linearly increases with n for $n < 0.4$, and the magnitude is nearly U independent. Thus, we made a linear extrapolation for the points of $n < 0.5$ to $n = 1$ ($\delta = 0$) in the n vs. $N_{\rm ingap}$ plot, and obtained the value N_0 for $La_{1-x}Sr_xTiO_3$ as the $n = 1$ ($\delta = 0$) intersection ($\sim$ 0.45). The value of N_0 for another R was determined by the relation $N_{0,R} = N_{0,\rm La} \times \tilde{W}$ ($\tilde{W} = W_R/W_{\rm La}$).

the result of cuprates and other 3d transition-metal oxides [30, 36, 43] and is consistent with several theoretical studies [44, 45, 46, 47] based on the Hubbard Hamiltonian. Solid lines are the result of least-square fitting to the function,

$$N_{\rm ingap}/N_0 = C\delta. \tag{3.7}$$

As can be seen in Fig. 3.6, the slope of the line, i.e., the C value, decreases with decrease of $\tilde{W}$. To check the possible dependence of $N_{\rm ingap}$ and C on the adopted value of ω_c, we also calculated $N_{\rm ingap}$ for $Nd_{1-x}Ca_xTiO_3$ with ω_c = 0.8 eV (open squares and the dashed line) instead of 1.1 eV, and found that the variation of C originated from the different ω_c values is not so large as to affect the discussion below.

Figure 3.7 shows the $\tilde{W}^{-1}$ (strength of electron correlation) dependence of C^{-1} (lower panel), where C is the rate of the Drude-part evolution with δ defined in Eq. (3.7), together with the value of $2\Delta/W$ and $2\Delta_{\rm act}/W$ (upper panel) discussed in the last section. Just as $2\Delta/W$, C^{-1} also decreases linearly with decrease of $\tilde{W}^{-1}$. The solid line in the lower panel is the result of a least-square fitting to the linear function. It is noteworthy that the value of $\tilde{W}^{-1}$ at which C^{-1} becomes zero is nearly the same as the value at which 2Δ becomes zero. This means that the evolution rate of the in-gap spectrum with δ is critically (divergently) enhanced as the strength of electron correlation (U/W) approaches the critical value of the bandwidth-control Mott transition $(U/W)_c$, following the relation,

$$C \propto [(U/W) - (U/W)_c]^{-1}. \tag{3.8}$$

According to the calculation of one dimensional Hubbard system using the Bethe ansatz for large U limit [45], $N_{\rm ingap}$ increases linearly with $\delta = 1-n$ for the small δ limit, and the coefficient C is given such as

$$C = \frac{\pi}{2}(1 + 2(\ln 2)\frac{W}{U}), \tag{3.9}$$

where $W = 4t$ in one-dimensional systems. However, this functional form shows no critical behavior at finite values of U/W, in contrast to the case of the present compounds. The calculation of two-dimensional Hubbard system using exact diagonalization method [44] indicates that the U/W dependence of C is qualitatively the same as that of the one dimension. The difference between our experimental result and the calculations in lower dimensions apparently comes from the difference of the magnitude of $(U/W)_c$ (critical values for the bandwidth-control Mott transition); $(U/W)_c$ is zero for the one or two dimensional systems (i.e., the ground state is always an insulator for $n = 1$ with non-zero U/W), while it is likely a finite value for the present compounds that is a three-dimensional system.

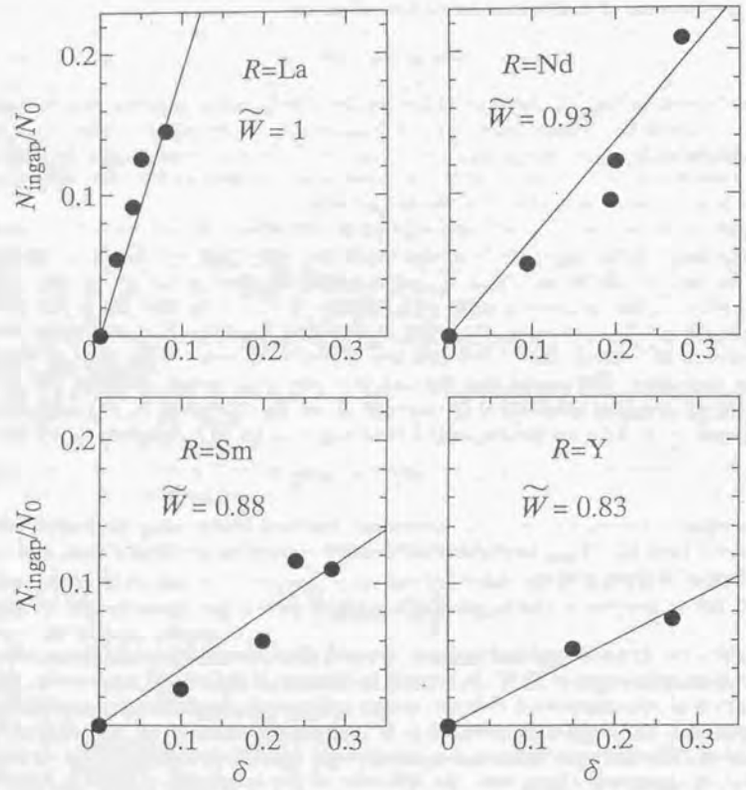

Figure 3.6: Effective number of electrons of the in-gap state ($N_{\rm ingap}$) normalized to that for $U = 0$ and $\delta = 0$ (N_0) as a function of δ for $R_{1-x}Ca_xTiO_3$ with R=La, Nd, Sm, and Y. Straight lines are the result of least-square fitting to the function $N_{\rm ingap}/N_0 = C\delta$.

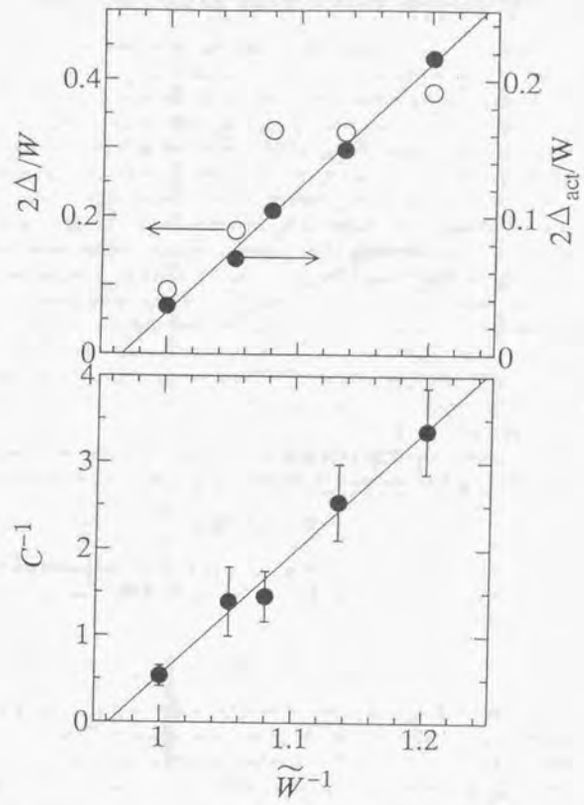

Figure 3.7: Upper panel: $\tilde{W}^{-1}$ dependence of 2Δ (an energy gap obtained by optical conductivity spectra) and $2\Delta_{\rm act}$ (two times activation energy obtained by the temperature dependence of resistivity) normalized to the bandwidth (W). The solid line is the result of least-square fitting of the data of $2\Delta_{\rm act}/W$ to the linear function. Lower panel: $\tilde{W}^{-1}$ dependence of C^{-1}, where C is the rate of the Drude-part evolution with δ defined in Eq. (3.7). The solid line is the result of least-square fitting to the linear function.

3.6 The insulating state with finite doping

The insulating phase not only exists at half-filling but also persists in the finite-doping region for the present Ti oxide. For example in $Nd_{1-x}Ca_xTiO_{3+y/2}$, the $\delta = 0$ sample shows activation-type temperature dependence of resistivity, and a clear gap-like structure in the optical conductivity spectrum, as indicated in Fig. 3.8. Such an insulating state comes from the on-site Coulomb interaction (i.e., being a Mott insulator) as described above. When the 9% holes are doped to this Mott insulator, the resistivity keeps on increasing with decrease of temperature, but its temperature dependence deviates from the activation type. In the optical conductivity spectrum, the in-gap state increases inside the Mott-gap structure of the $\delta = 0$ spectrum, but the magnitude of conductivity at zero energy remains almost zero. This type of an insulator with finite hole concentration cannot be explained by a simple Hubbard model that takes account of only on-site Coulomb interaction. For the 18%-doped sample, resistivity decreases with decrease of temperature, and the magnitude of conductivity at zero energy $[\sigma(\omega \sim 0)]$ becomes finite, i.e., the sample is metallic, although the shape of $\sigma(\omega)$ is not a simple Drude-type. Such an insulating phase away from the integer filling is widely observed in other transition metal oxides such as perovskite-type vanadates [30] and manganites.[48].

As discussed in Chapter 2, the critical hole concentration of the insulator-metal transition (δ_c) depends on the strength of electron correlation (Fig. 2.6) approximately as

$$\delta_c \propto (U/W) - (U/W)_c. \tag{3.10}$$

The experimental value for $(U/W)_c$ in Eqs. (3.7) and (3.10) is nearly identical as seen for the comparison between Fig. 3.7 and 2.6 in Chapter 2. Thus, we can derive a simple law from Eqs. (3.6), (3.7), and ((3.10)

$$N_c = C\delta_c = \text{const.} \tag{3.11}$$

The value of N_c corresponds to the spectral weight of the in-gap state that is required for metallic conduction. In other words, the in-gap state caused by hole doping does not contribute to the metallic conduction if its spectral weight is less than a certain value. In Fig. 3.9, we plot N_{ingap} as a function of δ for several R. Here, we plot insulating samples (in which $d\rho/dT$ is negative at all temperatures) as closed symbols and metallic ones as open symbols. This figure clearly shows the existence of the critical value N_c (~ 0.03) that separates the insulating and metallic regions, which does not depend on R or the critical hole concentration δ_c.

Keeping such a feature in mind, let us consider the possible origin of the insulating state with finite doping. One is that the random potential might localize the conduction carriers, i.e., Anderson localization.[1] Such an effect is observed in doped semiconductors, where the dopant itself acts as random potential and the sample remains insulating up

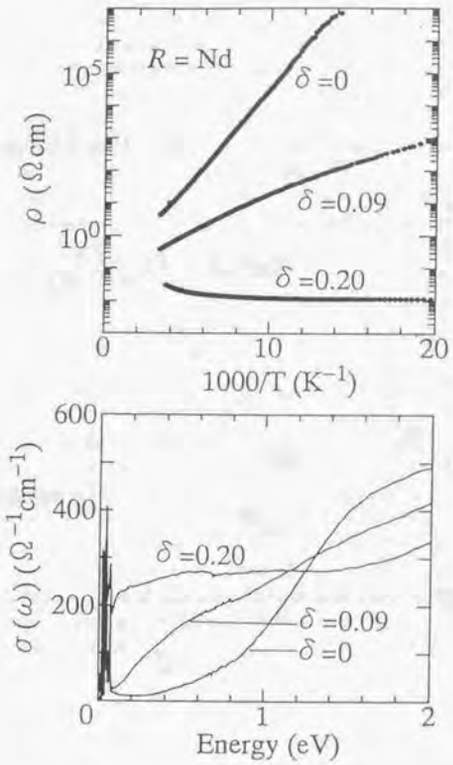

Figure 3.8: (a) ρ vs. T^{-1} for $Nd_{1-x}Ca_xTiO_{3+y/2}$ with $\delta = 0$, 0.09 and 0.20, and (b) optical conductivity spectra $\sigma(\omega)$ for the corresponding crystals.

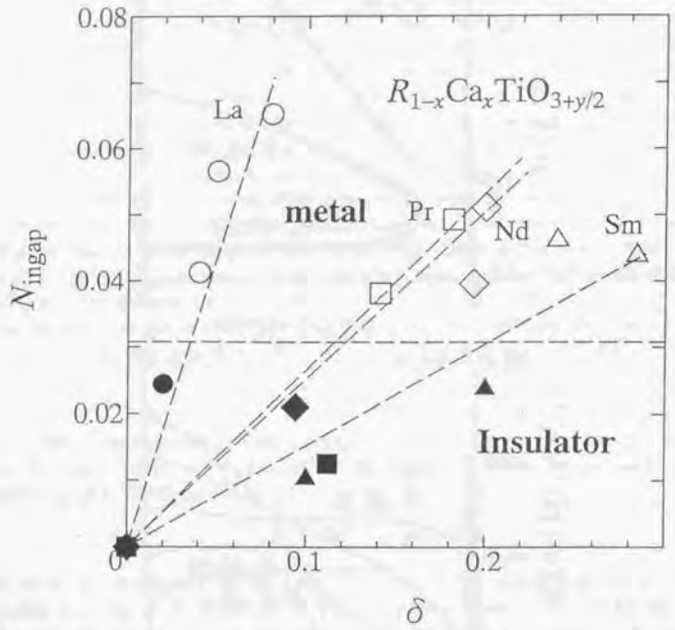

Figure 3.9: Spectral weight of the in-gap state ($N_{\rm ingap}$) as a function of δ for $R_{1-x}Ca_xTiO_{3+y/2}$. Closed symbols represent insulating crystals and open symbols the metallic ones. Circles, squares, rhombuses, and triangles represent R=La, Pr, Nd, and Sm, respectively. The dashed line indicates the critical value of $N_{\rm ingap}$ (~ 0.03) for the metal-insulator transition.

to critical doping concentration. In the present $R_{1-x}Ca_xTiO_{3+y/2}$ system, the trivalent R and divalent Ca forms a solid solution, which could act as random potential for the conduction carriers. Another possible origin for the insulating state is the electron-phonon interaction, by which conduction carriers could be localized as small polarons. In both cases, localization or delocalization of the conduction carriers depends on whether the transfer energy (bandwidth) for conduction carriers is smaller or larger than a critical value. In fact, Millis *et al.* [49] recently investigated the effect of electron-phonon interaction on conduction carriers by a dynamical mean field method, and found that thee resistivity shows a semiconducting behavior when a dimensionless parameter $\lambda = g^2/kt$ (t is the transfer energy of electrons, g the coupling constant of electron-phonon interaction, and k the elastic force constant) is larger than a critical value. Such scenarios are consistent with the abovementioned feature (existence of N_c), provided that the spectral weight of the in-gap state $N_{\rm ingap}$ represents the "renormalized" bandwidth for the carriers with strong electron correlation. In other words, doping controls such renormalized bandwidths, which increase proportionally with doping concentration, and the system becomes metallic when the hole concentration, and resultantly the renormalized bandwidth is larger than the critical value.

3.7 Summary

We investigated the optical spectra for $R_{1-x}Ca_xTiO_3$, varying the strength of electron correlation (U/W) as well as the band filling $n = 1 - \delta$. With decrease of n from 1 (increase of δ from 0), the spectral weight of the Mott-gap excitation is reduced and that of the in-gap state increases linearly. We found that the rate of the in-gap state devolution with δ is critically enhanced as U/W approaches the critical value of the bandwidth-control Mott transition for $n = 1$ [$(U/W)_c$], in the manner of $[U/W-(U/W)_c]^{-1}$. It was also found that the metal-insulator transition at a finite hole doping level in series of $R_{1-x}Ca_xTiO_{3+y/2}$ takes place when the spectral weight of the in-gap state in the optical conductivity spectrum reaches the common critical value.

Chapter 4

Optical spectra: temperature dependence

4.1 Introduction

In Chapter 3, the bandwidth and band-filling dependence of optical spectra are investigated for $R_{1-x}Ca_xTiO_{3+y/2}$ at room temperature in view of the effective number of electrons, which is the integrated value of the optical conductivity. In this chapter, we discuss the temperature dependence of the spectra with more quntitative analysis. In particular, we focus on the spectra for metallic crystals near the metal-insulator phase boundary. It is known that such samples show characteristic behaviors of the correlated metals,[13] such as enhanced specific-heat coefficient and Pauli susceptibility, and T^2 relation in resistivity. Furthermore, as described in Chapter 2, the crystal on the verge of the metal-insulator phase boundary shows antiferromagnetic ordering with metallic conduction at low temperature.

Here, two crystals are chosen for the optical spectroscopy. One is $CeTiO_{3+y/2}$, which shows a metallic behavior in resistivity but shows antiferromagnetic ordering at 70 K (the upper panel of Fig. 4.1). The other is $Ce_{0.95}Ca_{0.05}TiO_{3+y/2}$, which is a paramagnetic metal down to the lowest temperature (the lower panel of Fig. 4.1. In Fig. 4.2, a schematic phase diagram of the perovskite titanates as a function of T-δ is illustrated, in which positions of those compounds are shown by arrows.

4.2 Optical spectra in the PM phase

The upper panels of Fig. 4.3 show the temperature (T) dependence of reflectivity for $CeTiO_{3+y/2}$ above T_N = 70 K (left) and $Ce_{0.95}Ca_{0.05}TiO_{3+y/2}$ and (right). For both compounds, the reflectivity increases towards 100 % with decrease of energy at all temperatures,

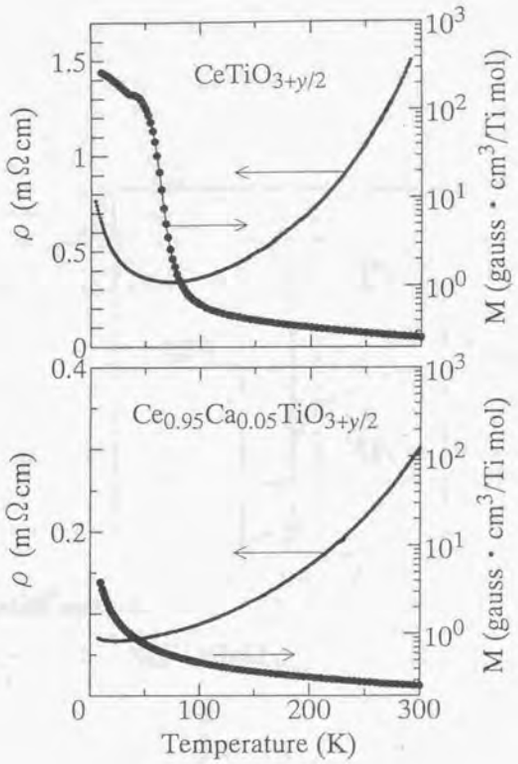

Figure 4.1: Resistivity (left axis) and magnetization at 100 Oe (right axis) as a function of T for $CeTiO_{3+y/2}$ (the upper panel) and $Ce_{0.95}Ca_{0.05}TiO_{3+y/2}$ (the lower panel).

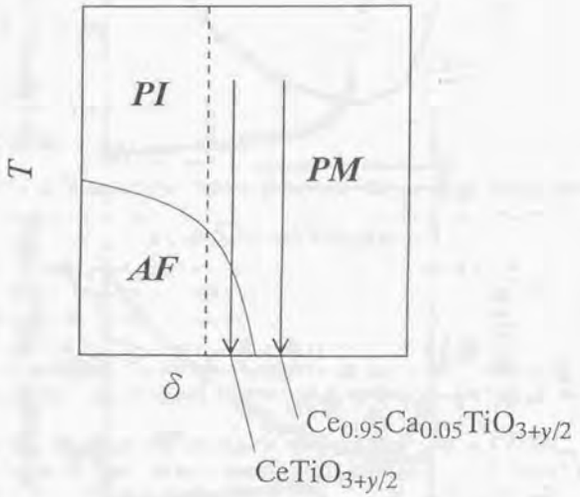

Figure 4.2: Schematic phase diagram of $R_{1-x}Ca_xTiO_{3+y/2}$ as a function of δ and T. PI, AF, and PM represent a paramagnetic insulating, antiferromagnetic, and paramagnetic metallic phase, respectively. Positions of $CeTiO_{3+y/2}$ and $Ce_{0.95}Ca_{0.05}TiO_{3+y/2}$ are shown by arrows.

which is a typical spectrum for metals. Comparing the spectra of the two compounds at the same T, the reflectivity of $Ce_{0.95}Ca_{0.05}TiO_{3+y/2}$ is higher than that of $CeTiO_{3+y/2}$. With decrease of T, the reflectivity increases for both compounds. Roughly speaking, higher reflectivity in a metallic phase corresponds to larger conductivity, and so, such hole-concentration dependence and T dependence of reflectivity is qualitatively consistent with behavior of their dc resistivity.

Optical conductivity spectra obtained from Kramers-Kronig transformations of the reflectivity are shown in the lower panel of Fig. 4.3. For $CeTiO_{3+y/2}$ (left), the spectrum at 290 K is rather a flat one which slightly increases with decrease of energy, accompanying sharp peaks below 0.1 eV corresponding to optical phonon modes. With decrease of T (above T_N), the low-energy conductivity (< 0.7 eV) increases whereas the high-energy conductivity decreases. On the other hand, the optical conductivity spectra for more metallic compound, $Ce_{0.95}Ca_{0.05}TiO_{3+y/2}$ (right), increases more sharply with decrease of energy than that for $CeTiO_{3+y/2}$. With decrease of T, the low-energy conductivity (< 0.4 eV) increases whereas the high-energy conductivity decreases, similarly to the T dependence of $CeTiO_{3+y/2}$.

The functional form of a simple metal is given by the Drude formula [50]

$$\frac{\omega_p^2}{4\pi}\frac{\tau}{1+\omega^2\tau^2} \tag{4.1}$$

where ω_p is the plasma frequency and τ the relaxation time of the conduction carriers. This function has a Lorentzian shape whose peak is centered at zero energy and whose integrated weight and width is given by $\omega_p^2/8$ and $1/\tau$, respectively. On the basis of this functional form, the experimental results can be qualitatively interpreted that the scattering rate $1/\tau$ increases with T, and that of $Ce_{0.95}Ca_{0.05}TiO_{3+y/2}$ is smaller than that of $CeTiO_{3+y/2}$ when they are compared at the same T. However, such a simple formula cannot completely reproduce the experimental spectrum.

For more quantitative discussion, we analyze the spectra by the extended Drude model,[51] where the energy dependence of the scattering rate and the effective mass is taken into account in the following way;

$$\begin{aligned}\sigma(\omega) &= \frac{\omega_p^2}{4\pi}\frac{\tau(\omega)}{1+[m^*(\omega)/m]^2\omega^2\tau(\omega)^2},\\ \epsilon_1(\omega) &= \epsilon_\infty - \omega_p^2\frac{[m^*(\omega)/m]\tau(\omega)^2}{1+[m^*(\omega)/m]^2\omega^2\tau(\omega)^2}.\end{aligned} \tag{4.2}$$

Here, $m^*(\omega)$ and $1/\tau(\omega)$ are the ω-dependent mass and the scattering rate of the conduction carriers, m the unrenormalized mass, and ω_p (unrenormalized plasma frequency) $= \sqrt{4\pi ne^2/m}$, where n is the density of carriers. We adopted the plasma frequency $\omega_p =$

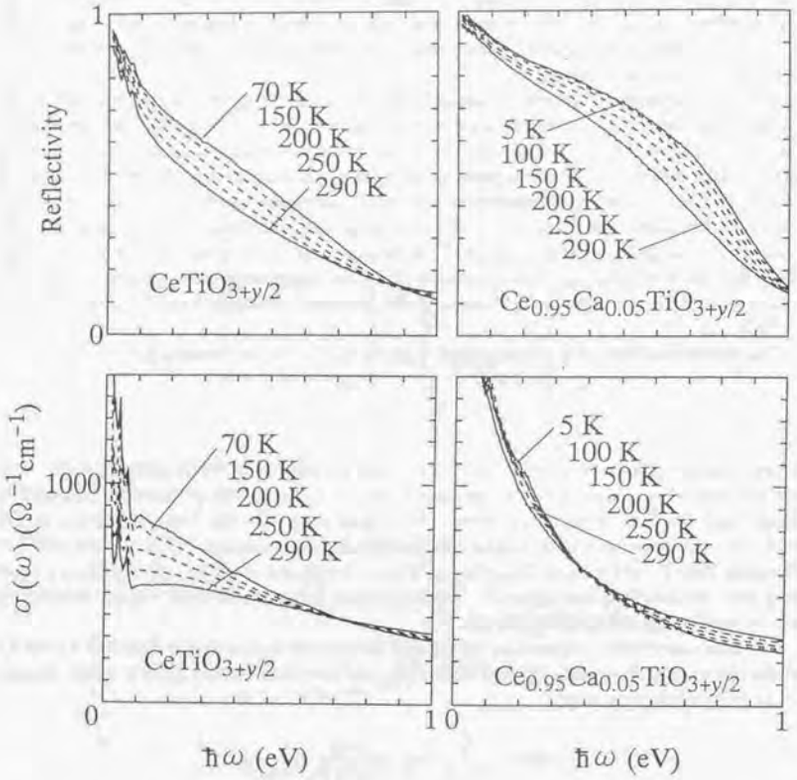

Figure 4.3: Reflectivity (the upper panel) and optical conductivity $\sigma(\omega)$ (the lower panel) spectra for $CeTiO_{3+y/2}$ (the left side) and $Ce_{0.95}Ca_{0.05}TiO_{3+y/2}$ (the right side). Note that only the spectra above $T_N = 70$ K are shown for $CeTiO_{3+y/2}$.

2.03 eV for $CeTiO_{3+y/2}$ and 2.25 eV for $Ce_{0.95}Ca_{0.05}TiO_{3+y/2}$ so that m^*/m becomes unity at 1 eV.

The result of the analysis is shown in Fig. 4.4. The m^*/m value (upper panel) is enhanced with decrease of ω for both compounds, though the enhancement is more pronounced for $CeTiO_{3+y/2}$. However, there is little T dependence of m^*/m. On the other hand, the scattering rate $1/\tau$ shows both ω and T dependence. It is notable that $1/\tau(\omega)$ shifts almost rigidly with T for both compounds. In other words, the magnitude of the change in $1/\tau$ with T does not depend on ω. To see these T dependence more clearly, we plot the value of $1/\tau$ at 0.1 eV and 0.5 eV for $Ce_{0.95}Ca_{0.05}TiO_{3+y/2}$ as a function of T^2 in Fig. 4.5. The $1/\tau$ values at $\omega = 0$ from the dc resistivity is also plotted, which is obtained from the relation $\sigma(\omega = 0) = (\omega_p^2\tau/4\pi)$ with the same plasma frequencyω_p as that used in the extended Drude analysis. The resistivity of this compound is known to show T^2 dependence as described in the previous section, and thus, $1/\tau(\omega = 0)$ becomes linear against T^2, as seen in Fig. 4.5. Such T^2 relation is also seen for $1/\tau$ at 0.1 eV and 0.5 eV, and the T^2 coefficient is almost identical with that at $\omega = 0$. This indicates that the T dependent part of $1/\tau$ does not depends on ω.

Such characteristic ω and T dependence of $1/\tau$ in these compounds can be described that $1/\tau(\omega, T)$ is the sum of the ω-dependent, the T-dependent, and the residual part,

$$\frac{1}{\tau(\omega,T)} = \frac{1}{\tau_0} + \frac{1}{\tau(\omega)} + \frac{1}{\tau(T)}. \tag{4.3}$$

This relation implies that the change of conductivity with T is dominated only by the $1/\tau(T)$ term from the dc value (0 eV) to ~ 1 eV. Moreover, the $1/\tau(T)$ is given by AT^2 below room temperature, and thus, only the value A is the relevant parameter dominating the temperature dependence of the conductivity.

We note that Eq. (4.3) is consistent with the T and energy dependence of the scattering rate of the conduction carriers in the Fermi-liquid theory.[52] In the Fermi-liquid theory, $1/\tau(\omega)$ and $1/\tau(T)$ should have ω^2 and T^2 dependence in the low ω / T limit, and the coefficient of T^2 in $1/\tau(T)$ is larger than that of ω^2 in $1/\tau(\omega)$ by a factor of π^2 (~ 9.8) [52]. The T^2 relation in $1/\tau(T)$ is clearly observed below 290 K in $Ce_{0.95}Ca_{0.05}TiO_{3+y/2}$ as described above (Fig. 4.5), and the coefficient is ~ 210 eV^{-1} from the dc value. On the other hand, $1/\tau(\omega)$ shows saturation behavior above ~ 0.1 eV for both compounds and appears to follow the ω^2 relation only below 0.1eV. The upper panel of Fig. 4.6 plots the $1/\tau$ as a function of ω^2 for $Ce_{0.95}Ca_{0.05}TiO_{3+y/2}$ at several temperatures. The closed circles shows the dc value of $1/\tau$ at the corresponding T. We can estimate the ω^2 coefficient as ~ 12 eV^{-1} (shown by the dashed straight line). Therefore, the ratio of the T^2 coefficient to the ω^2 coefficient is 17 in the experiment, which appears almost consistent with the theoretical value, allowing for the experimental error.

We also plot $1/\tau(\omega)$ as a function of ω^2 for $CeTiO_{3+y/2}$ at several temperatures (above T_N) in the lower panel of Fig. 4.6, together with the dc value (closed circles). It is rather

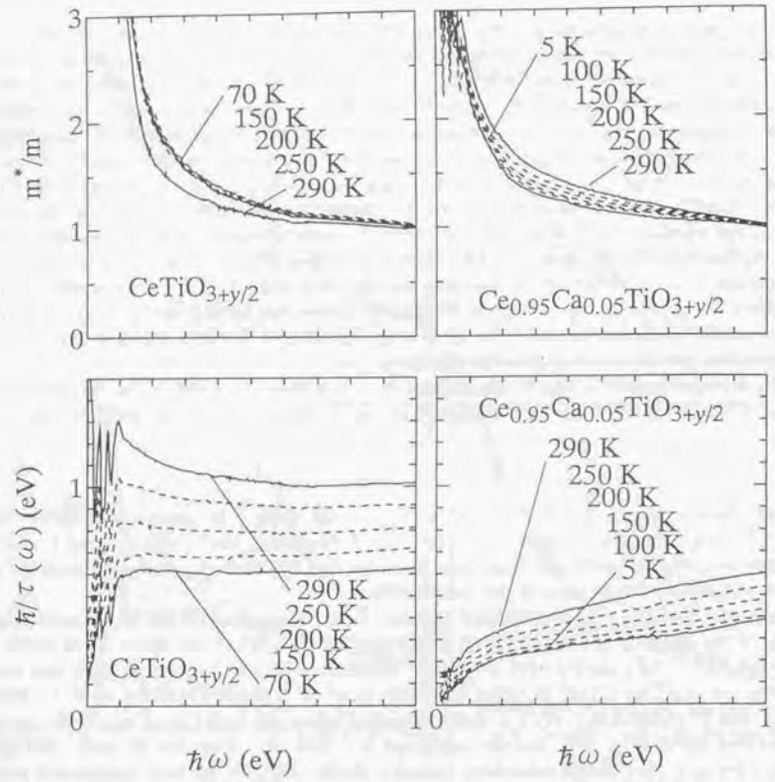

Figure 4.4: ω-dependent effective mass $m^*(\omega)$ (the upper panel) and scattering rate $\hbar/\tau(\omega)$ (the lower panel) from the extended Drude analysis for $CeTiO_{3+y/2}$ (the left side) and $Ce_{0.95}Ca_{0.05}TiO_{3+y/2}$ (the right side). $m^*(\omega)$ is normalized to the unrenormalized mass m (See text).

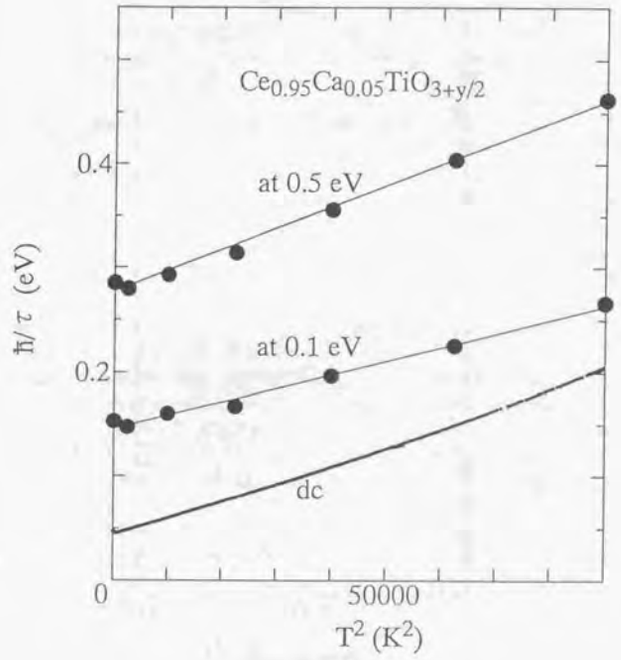

Figure 4.5: Scattering rate $\hbar/\tau$ at 0.1 eV, 0.5 eV from the extended Drude analysis, and the dc value of the scattering rate from conventional dc resistivity measurement, as a function of T for $Ce_{0.95}Ca_{0.05}TiO_{3+y/2}$. The dc value is obtained from the relation $\sigma(\omega = 0) = \omega_p^2\tau/4\pi$ with the same plasma frequency as that used in the extended Drude analysis.

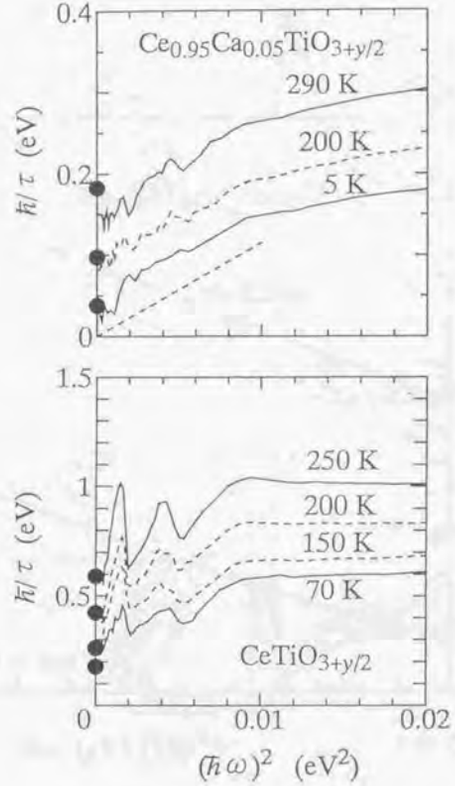

Figure 4.6: ω-dependent scattering rate $\hbar/\tau(\omega)$ as a function of the $(\hbar\omega)^2$ at several temperatures for $Ce_{0.95}Ca_{0.05}TiO_{3+y/2}$ (the upper panel) and $CeTiO_{3+y/2}$ (the lower panel). Closed circles represent the dc scattering rate estimated from the dc resistivity. The dashed line in the upper panel is for the estimation of the ω^2 coefficient in $\hbar/\tau(\omega)$.

difficult to quantitatively estimate the ω^2 coefficient in $1/\tau(\omega)$ from this figure, due to the structures arising from optical-phonons below 0.1 eV. Further, the dc resistivity (the dc scattering rate) does not completely obey the T^2 relation even above T_N for $CeTiO_{3+y/2}$. Qualitatively speaking, both the slope of the $\omega^2-1/\tau(\omega)$ curves at $(\hbar\omega)^2 < 0.01$ eV^2 (shown in Fig. 4.5 and the slope of the $T-\rho$ curves (shown in Fig. 4.1) are several times larger for $CeTiO_{3+y/2}$ than for $Ce_{0.95}Ca_{0.05}TiO_{3+y/2}$, indicating that the ratio of the T^2 coefficient to the ω^2 coefficient is not so much different between two compounds. This implies that the Fermi-liquid picture holds good for this perovskite titanates even in the vicinity of the metal-insulator phase boundary in the paramagnetic metallic phase.

4.3 Comparison with other systems

It is interesting to compare the ω- and T-dependent scattering rate $1/\tau(\omega,T)$ and effective mass $m^*(\omega,T)$ of the present titanates with those of the cuprate, which is another typical doped-Mott system and is known to show non-Fermi-liquid-like behaviors. A notable result of the extended Drude analysis for the cuprate [40, 41] is the anomalous temperature dependence of $1/\tau(\omega)$ in the underdoped region in the normal state. For Bi2212 in the underdoped region (T_c = 67 K),[40] for example, $1/\tau(\omega)$ is suppressed below 800 cm^{-1} with decrease of temperature (above T_c), whereas it is almost T-independent above that frequency, as shown in Fig. 4.7. Such a suppression of $1/\tau(\omega)$ with decreasing T only at the low-ω region is qualitatively different from the uniform change of $1/\tau(\omega)$ against ω for the present titanate, but is similar to the spectral change observed in the superconducting state of the same compound. This suggests that a pseudogap exists for the underdoped cuprate even in the normal state. On the other hand, the $1/\tau(\omega)$ spectra for the overdoped Tl2201 (T_c = 23 K) shows a rigid shift with a change of T, which is similar to the behavior of the present titanates.

Therefore, a crossover from the Fermi-liquid-like behavior to the non-Fermi-liquid-like behavior (pseudogap behavior) with decrease of hole concentration is a characteristic feature in the optical spectra of cuprates. On the contrary, for the present titanate, both $CeTiO_{3+y/2}$ (smaller hole concentration), which is located on the verge of the metal-insulator transition, and $Ce_{0.95}Ca_{0.05}TiO_{3+y/2}$ (larger hole concentration) show Fermi-liquid-like behavior in the paramagnetic metallic phase. In other words, the titanate shows the Fermi-liquid-like behavior for any hole concentration in the paramagnetic metallic region, and that is in contrast to the behavior of the cuprates.

Another example that shows anomalous behavior in $1/\tau(\omega,T)$ and $m^*(\omega,T)$ is the heavy-Fermion compounds. A typical one is URu_2Si_2,[53] in which $m^*(\omega)$ is enhanced and $1/\tau(\omega)$ is suppressed below 100 cm^{-1} with decreasing T below 70 K, where the conduction carriers show coherent motion and resistivity drops with decreasing T (Fig. 4.8). Such renormalization of the low-energy effective mass and scattering rate is responsible for the enhanced

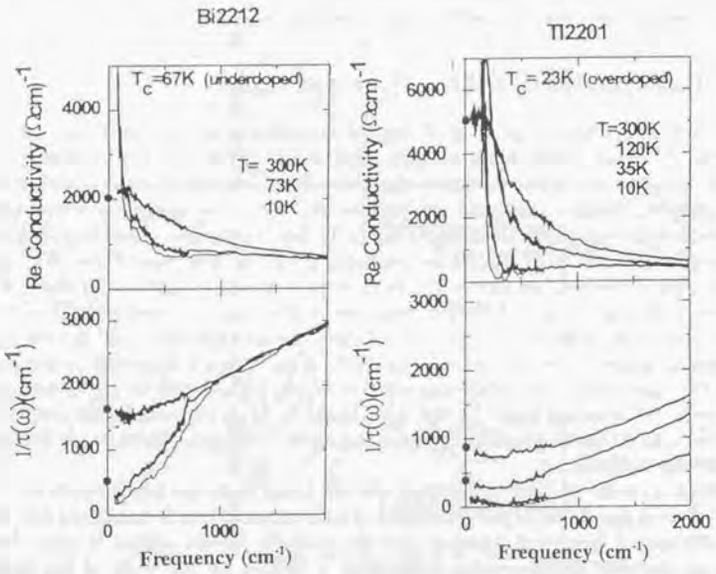

Figure 4.7: Optical conductivity spectra (the upper panel) and scattering rate $1/\tau(\omega)$ (the lower panel) for Bi2212 in the underdoped region ($T_c = 67$ K, the left side) and for Tl2201 in the overdoped region ($T_c = 23$ K, the right side). (From Ref. [40])

specific-heat coefficient by a factor of 25 at the lowest temperature in this compound. We note that a similar behavior is observed for the c-axis spectrum of the quasi-two-dimensional compound Sr_2RuO_4,[54] (Fig. 4.9), which shows superconductivity below 1 K.

Compared with those compounds, the present titanates show the enhancement of the effective mass $m^*(\omega)$ at low energy (shown in Fig. 4.4), together with the enhancement of specific-heat coefficient [13, 17], but do not show any temperature dependence of $m^*(\omega)$, at least below 290 K. Such difference between the titanates and heavy-Fermion compounds appears to come from the different T and ω scale that dominates the electronic structures between these two systems. In URu_2Si_2, the enhancement of $m^*(\omega)$ is seen only below 100 cm^{-1} and the temperature dependence of $m^*(\omega)$ is observed below 70 K, as seen in Fig. 4.8. On the other hand, the enhancement of $m^*(\omega)$ of the titanates is observed below ~ 0.2 eV as shown in Fig. 4.4, whose energy scale is at least one order of magnitude larger than that of URu_2Si_2. Thus, the temperature range where the temperature dependence of $m^*(\omega)$ is seen in this titanates is expected to be higher than the room temperature. In this sense, transport and optical measurements at higher temperatures than the present work would be helpful to understand the renormalization of the effective mass and the scattering rate of the perovskite titanates.

4.4 Optical spectra in the AF phase

$CeTiO_{3+y/2}$ undergoes the antiferromagnetic-ordering transition at $T_N = 70$ K. Resistivity takes the minimum at that temperature, and keeps on increasing with further decrease of T, as shown in the upper panel of Fig. 4.1.

Reflectivity and the low-energy conductivity also decreases with decreasing T below T_N as shown in Fig. 4.10, which is consistent with the T dependence of the resistivity. However, the optical conductivity spectrum (the lower panel of Fig. 4.10) at the lowest T (5 K) does not show a gap-like structure, but smoothly increases with decrease of ω, except for the optical-phonon structures below 0.1 eV. Moreover, the value of the dc conductivity almost coincides with that of the optical conductivity at the lowest energy of the present measurement (~ 0.01 eV), and thus, it is unlikely that a gap-like structure is present below 0.01 eV. Therefore, optical spectrum for $CeTiO_{3+y/2}$ below T_N is that of a metal with no gap-like structure.

The extended-Drude analysis was applied to the metallic spectra below T_N and results are shown in Fig. 4.11. The effective mass $m^*(\omega)$ shows little T dependence, indicating that the spectral weight contributing metallic conduction barely decreases below T_N. On the other hand, the scattering rate $1/\tau(\omega)$ increases with decrease of T. It is notable that the change of $1/\tau(\omega)$ with T is not uniform against ω, but $1/\tau(\omega)$ increases larger for smaller ω. That is qualitatively different from the behavior above T_N, where $1/\tau(\omega)$ changes uniformly against ω. This suggests that the change of $1/\tau(\omega)$ with T is dominated by different origins

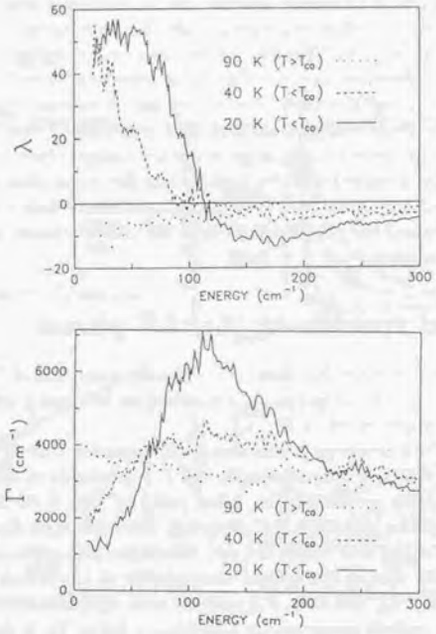

Figure 4.8: The enhancement of the effective mass λ ($= m^*/m - 1$ in our notation) and scattering rate Γ ($= 1/\tau$ in our notation) of URu_2Si_2 from the extended Drude analysis. (From Ref. [53])

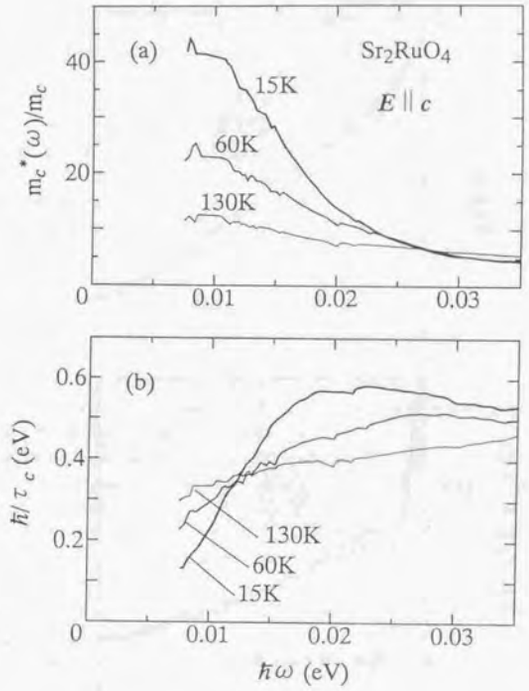

Figure 4.9: ω-dependent effective mass and scattering rate of Sr_2RuO_4 from the extended Drude analysis of the out-of-plane spectra. (From Ref. [54])

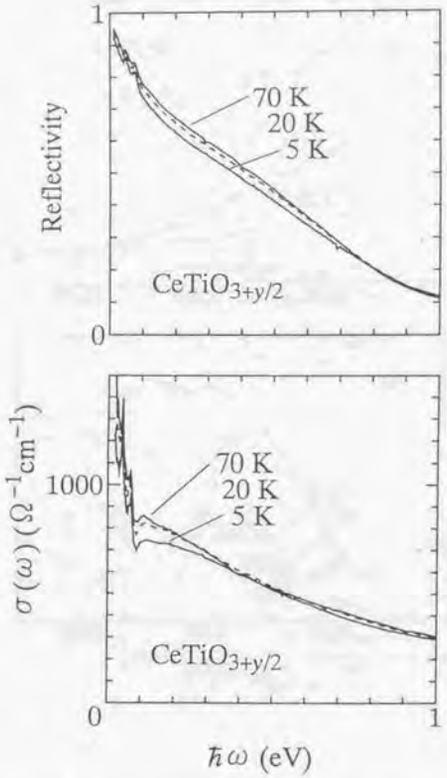

Figure 4.10: Reflectivity (the upper panel) and optical conductivity (the lower panel) for $CeTiO_{3+y/2}$ in the antiferromagnetic phase below 70 K.

above and below T_N.

There are various examples that show antiferromagnetic ordering in a metallic phase. A famous one is Cr metal,[55, 56] which becomes the spin-density-wave (SDW) state below 312 K due to the nesting of the Fermi surface. Associated with the SDW transition, optical conductivity [57] of Cr decreases below 1000 cm^{-1} whereas increases above that frequency, making up a gap-like structure, as shown in Fig. 4.12. Similar gap-like structures in the optical conductivity spectra of the SDW state were also observed for URu_2Si_2,[53] $(TMTSF)_2PF_6$,[58] and so on. Recently, a similar change of the optical conductivity with decreasing T has been observed for $Nd_{1.83}Ce_{0.17}CuO_4$,[59] which shows barely metallic conduction but also antiferromagnetic ordering below 150 K.

The absence of such a gap-like structure in the optical spectrum of the present titanate can be explained in several ways: One explanation is based on the SDW model just as the case of Cr metal, but assumes that a very small part of the Fermi surface disappears by the SDW gap formation. Accordingly, missing spectral weight with the gap formation is so small so that the gap-like structure is hardly observed experimentally in the optical spectrum. In such a case, the staggered moment induced by the SDW state would be orders of magnitude smaller than the full moment $Ti^{3+} \sim 1\mu_B$. So far, there is no neutron scattering measurement of the perovskite-type titanate that shows both metallic conduction and antiferromagnetic ordering. Measurement of the pattern of the spin-ordering as well as the magnitude of the ordered moment of such compounds would give a crucial test for that scenario of their antiferromagnetic ordering.

Another possible scenario is to take account of the two different kinds of electrons, one of which acts as conduction carriers and the other of which acts as localized spins. If the antiferromagnetic ordering occurs only for the localized spins, and conduction carriers are affected only through the interaction with such localized spins, one could expect the that the fluctuation of the ordered spins scatters the conduction carriers and thus increase of their scattering rate below T_N, as observed in the experiment.

In the present titanates, the conduction carriers are accommodated in the triply degenerated Ti $3d$ t_{2g} orbitals. As a result, there should be three different Fermi surfaces in the band structure of the cubic $RTiO_3$,[60] two of which have lighter effective mass and the rest of which has heavier effective mass. Thus, one can expect for the crystal near the metal-insulator phase boundary that electrons with lighter effective mass are delocalized and act as conduction carriers, whereas those with heavier effective mass are localized due to the electron-correlation effect and act as localized moments. We note that a preliminary study [61] indicates that the Hall coefficient of the crystal in the vicinity of the metal-insulator phase boundary is larger (suggesting smaller carrier number) than that of the crystal sufficiently away from the boundary. The staggered moment is not necessarily much smaller than $1\mu_B$ in this scenario, since it is approximately determined by the ratio of the number of localized spins and conduction carriers. On the basis of this scenario, however, the optical conductivity spectrum is the sum of the contribution from conduction

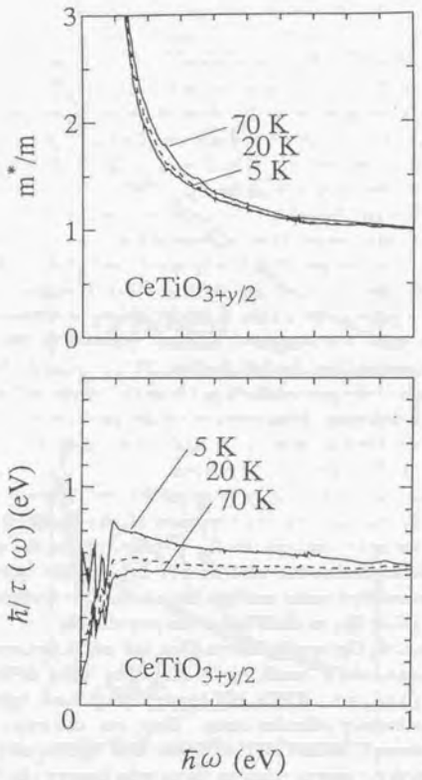

Figure 4.11: ω-dependent effective mass $m^*(\omega)$ (the upper panel) and scattering rate $\hbar/\tau(\omega)$ (the lower panel) in the antiferromagnetic phase.

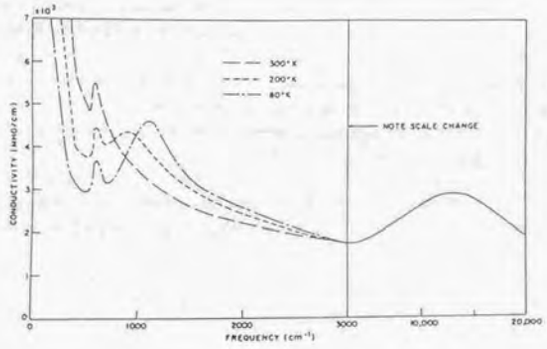

Figure 4.12: Optical conductivity of Cr metal. (From Ref. [57])

carriers (producing a Drude-like spectrum) and that from localized carriers (producing a broad peak). Such a feature is not compatible with the extended Drude analysis above, which is essentially a one-component model.

4.5 Summary

Temperature dependence of optical spectra were investigated for $CeTiO_{3+y/2}$, which shows metallic conduction but antiferromagnetic ordering at 70 K, and $Ce_{0.95}Ca_{0.05}TiO_{3+y/2}$, which is a paramagnetic metal down to the lowest temperature. Extended Drude analysis has revealed that temperature dependence of the conductivity in the paramagnetic phase can be attributed to the uniform change of the scattering rate of conduction carriers $1/\tau(\omega)$ against ω, whereas the effective mass $m^*(\omega)$ is almost T independent. Such a change of $1/\tau(\omega)$ with T is consistent with the Fermi-liquid theory, but in contrast to the behavior of the cuprate supereonductors. On the other hand, optical conductivity of $CeTiO_{3+y/2}$ in the antiferromagnetic phase is decreased in the low-energy region with decreasing T, but does not show any gap-like structure even at the lowest temperature. Such a spectral change suggests that the spectral weight contributing the metallic conduction barely decrease with antiferromagnetic ordering, but the scattering rate $1/\tau(\omega)$ increases in the low-energy region.

Chapter 5

Raman spectra

5.1 Introduction

Raman-scattering measurement is known as a powerful technique to investigate optical phonon modes, especially in insulators. The phonon spectrum in Raman scattering of insulators is dominated by the coupling between the phonon and electron-hole pairs created by an *interband* excitation [62]. On the other hand, Raman-scattering is also useful to investigate the electronic excitation of metals. In that case, the light emits the *intraband* electron-hole pair across the Fermi surface. Such electronic Raman spectra have experimentally been observed in various compounds [62], including the present perovskite-type titanates [63].

In this chapter, we describe systematic investigation of the phonon Raman spectra of the perovskite-type titanate. We have found that the phonon spectra show up only in the metallic region, and that the intensity of these spectra closely relates to the value of carrier effective mass, which critically increases as the MI phase boundary is approached. This indicates that such phonon modes are dominated by the coupling between the phonon and the *intraband* electron-hole pairs across the Fermi surface of the metallic state. We discuss quantitative relation between the phonon intensity in Raman spectra and the electronic parameters of metals.

5.2 Experiment

A 514.5 nm line from an argon ion laser was used as an incident light, whose intensity was typically 30 mW, and it was focused on the sample surface by a convex lens into the ~ 0.2 mmϕ spot. The scattered light in a nearly backward-scattering geometry was collected and dispersed by a triple monochromator equipped with an intensified-diode-array detector. Two polarizers for the incident and scattered light were used for selecting the

specific polarization configuration. A schematic figure of the measurement system is shown in Fig. 5.1. All the spectra were calibrated to the instrumental sensitivity as well as to the penetration depth of the incident and scattered light using optical constants obtained from the Kramers-Kronig analysis of the reflectivity spectra, so that we can compare the relative spectral intensity between different samples.

5.3 Phonon spectra in Raman scattering

We show the Raman-scattering spectra of (a) $La_{1-x}Sr_xTiO_{3+y/2}$ and (b) $Y_{1-x}Ca_xTiO_{3+y/2}$ at 50 K for the polarized configuration, in which the polarization of an incident and scattered light are parallel, in Fig. 5.2 . We clearly see some phonon peaks, shown by triangles in the figure, for the metallic samples for $\delta \geq 0.04$ in R=La and for $x \geq 0.45$ in R=Y. By contrast, the phonon peaks almost disappear in the insulating phase, for $\delta = 0.01$ in R=La, and for $x \leq 0.37$ in R=Y. Namely, the phonon Raman intensities show a critical change upon the MI transition.

The compounds, $La_{1-x}Sr_xTiO_{3+y/2}$ for $x \leq 0.3$ and $Y_{1-x}Ca_xTiO_{3+y/2}$ for all x, have orthorhombically distorted perovskite ($GdFeO_3$-type) structures [11, 14] in which the size of the unit cell is $\sqrt{2}a_p \times \sqrt{2}a_p \times 2a_p$ (a_p being the lattice spacing in the simple cubic perovskite structure). Therefore, several Raman-active phonon modes ($7A_{1g} + 7B_{1g} + 5B_{2g} + 5B_{3g}$) should exist according to the group theory analysis [64] for the samples whose spectra are shown in Figs. 5.2 (a) and (b). On the other hand, $La_{1-x}Sr_xTiO_{3+y/2}$ for $x > 0.4$ has a cubic perovskite structure [11] with no Raman-active mode, and we observed the disappearance of phonon structures for $x > 0.4$ associated with such an orthorhombic-cubic transition, as shown in Fig. 5.3. This indicates that the phonon structures shown in Fig. 5.2 (a) and (b) are not the disorder-induced modes but intrinsically Raman-active phonon modes inherent in the distorted perovskite structure.

We also measured the depolarized configuration spectra, in which the polarization of an incident light is perpendicular to that of a scattered light. As shown in Fig. 5.4, the phonon peaks between 200–400 cm^{-1} (indicated by closed triangles) weaken but those below 200 cm^{-1} (indicated by open triangles) remain strong as well in their intensity. It is thus apparent that the phonon modes between 200–400 cm^{-1} the A_{1g} symmetry. On the other hand, the phonon structure at 200 cm^{-1} is composed of the A_{1g} mode and other symmetry modes (as B_{1g}, B_{2g}, or B_{3g}) with nearly degenerated frequencies.

Figure 5.5 shows the A_{1g} phonon spectra between 200–400 cm^{-1} for R=Pr, Nd, and Sm at 50 K. The metal-insulator phase boundary is shown by a dashed line for each R series, and the intensity of these phonon spectra shows a critical change upon the MI transition also for R=Pr, Nd, and Sm.

Let us consider possible consequence of the x-dependent changes in the lattice structure. X-ray measurements [11, 14, 65] revealed that the orthorhombicity of these systems in-

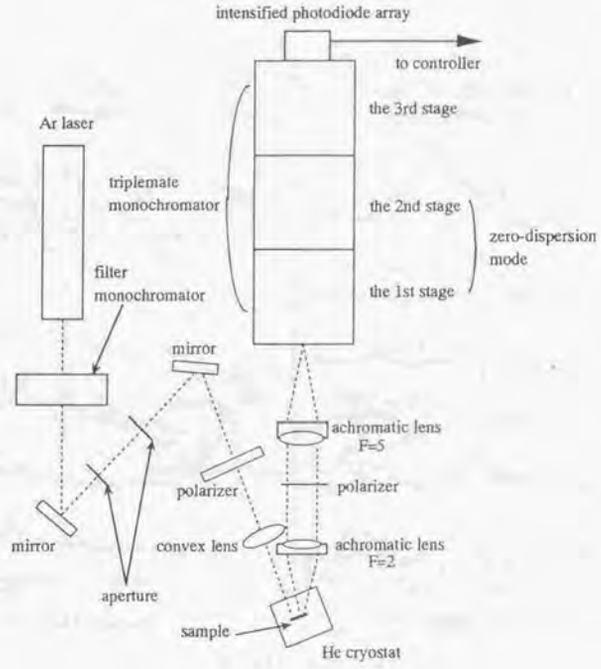

Figure 5.1: A Schematic figure of the measurement system for Raman scattering.

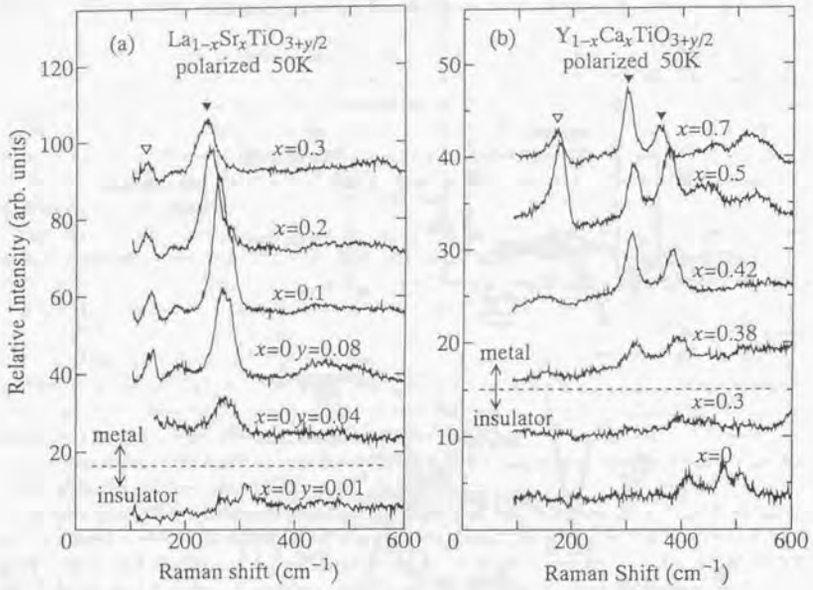

Figure 5.2: Raman-scattering spectra at 50K for the polarized configuration (in which the polarization of an incident and scattered light are parallel) of (a) $La_{1-x}Sr_xTiO_{3+y/2}$ and (b) $Y_{1-x}Ca_xTiO_{3+y/2}$. The scales of the y axis are in arbitrary units, but the relative intensity for all the spectra is valid. The spectra have been offset for clarity. Dashed lines represent the metal-insulator phase boundary of each series.

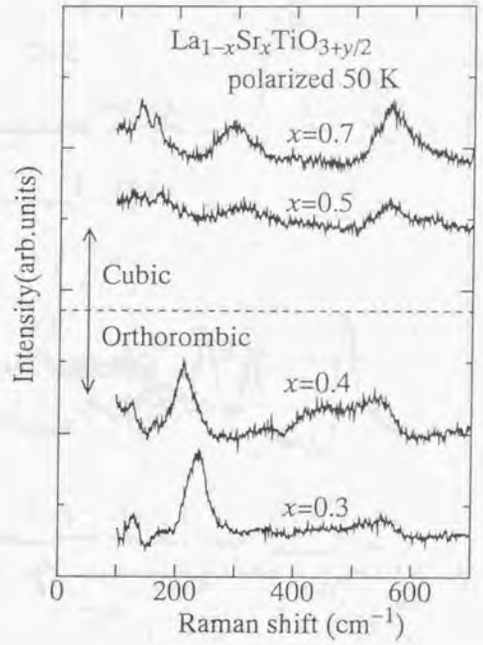

Figure 5.3: Raman-scattering spectra of $La_{1-x}Sr_xTiO_{3+y/2}$ with a cubic ($x \geq 0.5$) and orthorhombic ($x \leq 0.4$) lattice at 50 K for the polarized configuration.

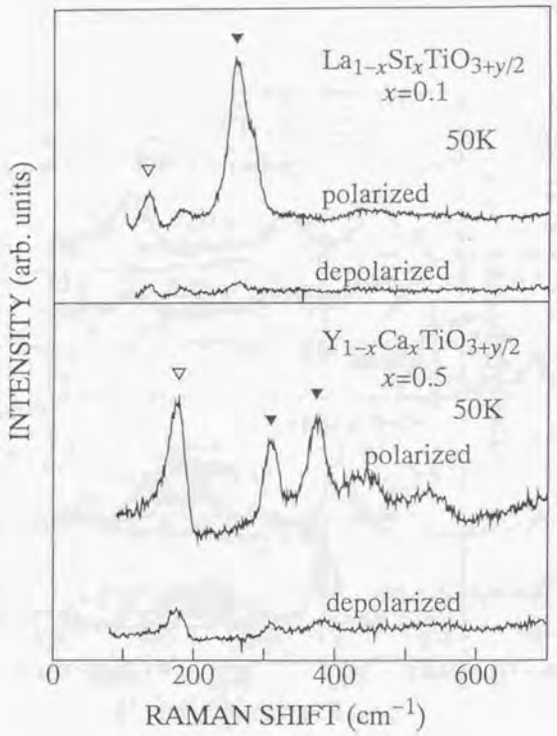

Figure 5.4: Comparison between the polarized (in which the polarization of an incident and scattered light are parallel) and depolarized (in which the polarization of an incident and scattered light are perpendicular) spectra for $La_{1-x}Sr_xTiO_{3+y/2}$ with $x = 0.1$ (the upper panel) and $Y_{1-x}Ca_xTiO_{3+y/2}$ with $x = 0.5$ (the lower panel) at 50 K.

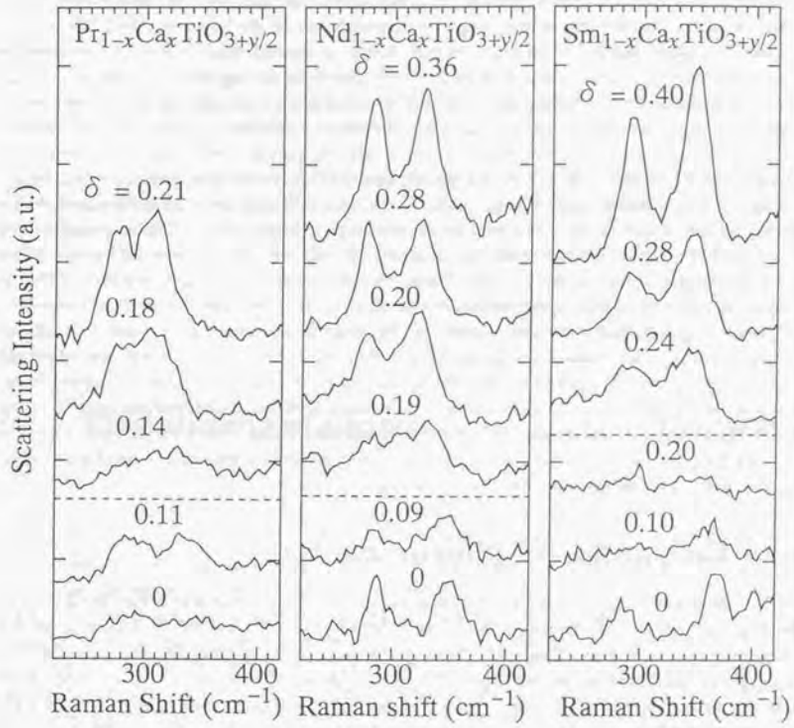

Figure 5.5: the A_{1g} phonon spectra between $200 - -400$ cm^{-1} for R=Pr, Nd, and Sm at 50 K. Dashed lines represent the metal-insulator phase boundary of each R series.

creases as x decreases. Such an x-dependent structural change would lead to the increase of spectral intensity of Raman-active phonon mode with decrease of x, because the phonon mode of interest becomes Raman-active exactly owing to the orthorhombic distortion. This prediction is, however, in contradiction with the experimental result that the phonon intensity rather decreases as x decreases, indicating that the change of the magnitude of the lattice distortion is not the major origin for the variation of the phonon intensity.

Another possible origin of such a spectral change is the resonance effect of the incident (or scattered) light, where the Raman intensity becomes strong if the energy of the incident/scattered light coincides with the strong absorption peak of the optical spectrum. This effect is in fact the most dominant for the phonon Raman intensity of conventional band insulators. In this system, however, the lowest electronic level with a large oscillator strength, which is the O $2p$-Ti $3d$ charge transfer (CT) excitation at ~ 4.0 eV [11, 14], is too far for the incident light energy (2.41 eV) to be resonated with, as shown in Fig. 5.6 for R=La and Y series. Furthermore, the spectral position of the CT excitation depends x rather little, as exemplified in the same figure with the spectra for metallic (solid lines) and insulating (dashed lines) crystals. Thus, we can conclude that the resonance effect is not the cause of the observed variation of the phonon spectral intensity in the titanates.

Considering the fact that the change of the phonon intensity is correlated with the MI transition for five different R series with different MI phase boundaries, the observed behavior should be attributed to the change of the electronic state near the Fermi level. In other words, the phonon mode is strongly coupled with the *intraband* excitation across the Fermi level, and much less with the *interband* excitation. Such a coupling with the intraband excitation is allowed only in the metallic state but not in the insulating state with a charge gap larger than the phonon energy.

5.4 Calculation of phonon modes

For the assignment of the phonon modes observed in the Raman spectrum (mainly with the A_{1g} symmetry), calculation of the phonon frequency was made for R=La using a force constant model: At first, three stretching force constants between the nearest neighbor Ti-O, O-O, and La-O atoms were assumed in a cubic perovskite lattice. The magnitude of these force constants (55 Nm^{-1} for Ti-O, 35 Nm^{-1} for O-O, and 35 Nm^{-1} for La-O) were determined to reproduce the frequency of the three infrared-allowed modes in a cubic perovskite structure, which had experimentally been obtained as 166cm^{-1}, 337cm^{-1}, and 560cm^{-1} for $LaTiO_{3.00}$. [1] Then, Raman-allowed modes with the A_{1g} symmetry were calculated taking account of the $GdFeO_3$-type distortion of the $LaTiO_3$. In Fig. 5.7, the

[1]Here, the $GdFeO_3$-type distortion of this compound is ignored. In fact, splitting and apperance of phonon modes due to the $GdFeO_3$-type distortion is negligible in the optical conductivity spectrum of $LaTiO_{3.00}$, as shon in the lower panel of Fig. 5.7.

results of the calculation (the upper panel), together with the experimental spectra (the lower panel) of $LaTiO_{3.00}$ for the optical conductivity spectrum (the dashed line) and of $LaTiO_{3.04}$ for the Raman-scattering spectrum (the solid line) are presented. [2] Normal coordinates of the A_{1g} phonons from the calculation are shown in Fig. 5.8.

As can be seen in these figures, Raman-allowed modes below 200 cm^{-1} corresponds to the modes 1 and 2, in which La atoms mainly move ("rare-earth mode"). The 280cm^{-1} structure in the $LaTiO_{3.04}$ spectrum, which is composed of two peaks judging from the spectra of other R, corresponds to the modes 3 and 4 in the calculation, in which the TiO_6 octahedra is rigidly tilting ("tilting mode"). On the other hand, the calculated modes 5, 6, and 7, where TiO_6 octahedra is distorted ("distortion mode"), are hardly seen in the experimet.

Therefore, among the seven A_{1g} modes, the rare-earth modes and the tilting modes have strong intensity whereas the distortion modes have weak intensity in the Raman-scattering spectrum of the present titanates in the metallic phase. Since the rare-earth modes could be strongly affected by the disorder arising from the mixed R/Ca(Sr), we avoid the quantitative discussion of the rare-earth modes, but focus on the behavior of the tilting modes below. The reason why the intensity of the rare-earth modes and the tilting modes is strong whereas that of the distortion modes is weak is qualitatively discussed in the latter section.

5.5 The intensity of phonon Raman spectrum in metals

Figure 5.9 shows the integrated intensity of the tilting modes with the A_{1g} symmetry as a function of δ for R=La and Y. The dashed lines indicate the MI phase boundary, as determined by the resistivity measurement. As clearly seen, the spectral intensity of these modes in the metallic regions decreases as the MI phase boundary is approached, and almost disappears in the insulating regions for both La and Y series.

Figure 5.10 shows the three-dimensional plot of the intensity of the same modes as a function of δ and U/W (which depends on the species of R) for five different R systems, including Pr, Nd, and Sm series. The δ range of the insulating state (the shade area) increases with increasing U/W (with smaller ionic radius of R), as discussed in detail in the previous chapter. Nevertheless, the spectral intensity in the metallic phase decreases almost to zero as the MI phase boundary is approached for any R series.

Raman scattering in metals was theoretically studied by Mills, Maradudin, and Burstein (MMB) [66]. According to their theory, the scattering cross section of even parity phonon,

[2]We assume that phonon frequencies are not different between $LaTiO_{3.00}$ and $LaTiO_{3.04}$.

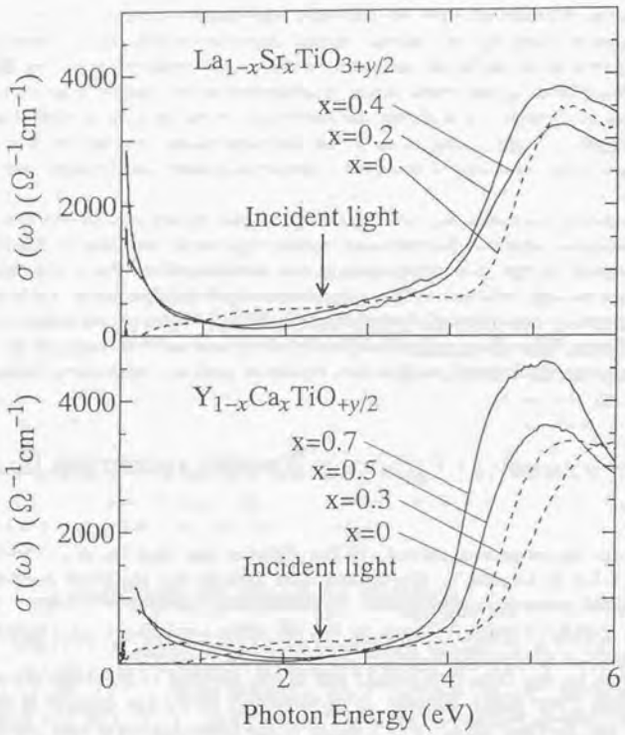

Figure 5.6: Plot of the optical conductivity spectra $[\sigma(\omega)]$ for $La_{1-x}Sr_xTiO_{3+y/2}$ (the upper panel) and $Y_{1-x}Ca_xTiO_{3+y/2}$ (the lower panel) with various hole concentrations, together with the energy position of the incident light of Raman scattering (shown by arrows).

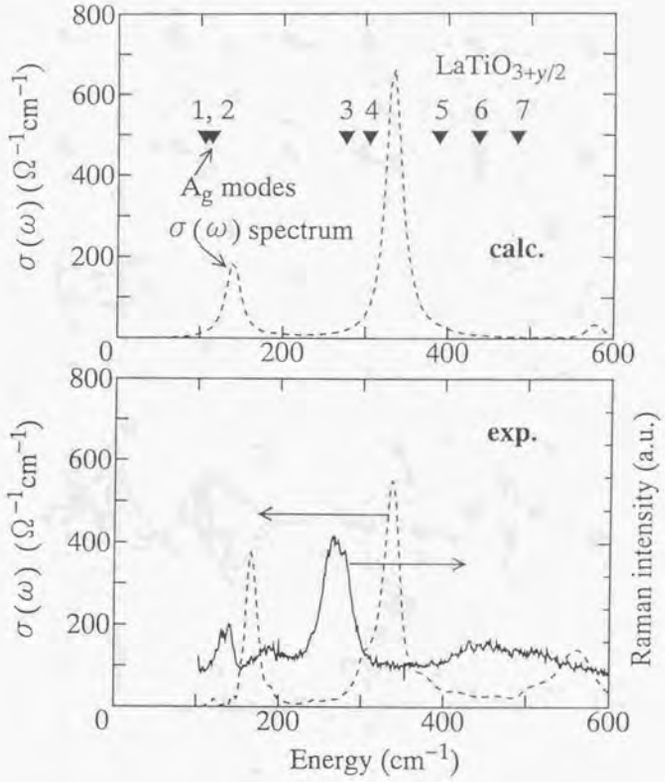

Figure 5.7: The upper panel: $\sigma(\omega)$ spectra of optical phonons (the dashed line) and frequency positions of the A_{1g} modes (shown by triangles) by the calculation (see text). The lower panel: the optical conductivity spectrum of $LaTiO_{3.00}$ (the dashed line) and the Raman-scattering spectrum of $LaTiO_{3.04}$ (the solid line) in the experiment.

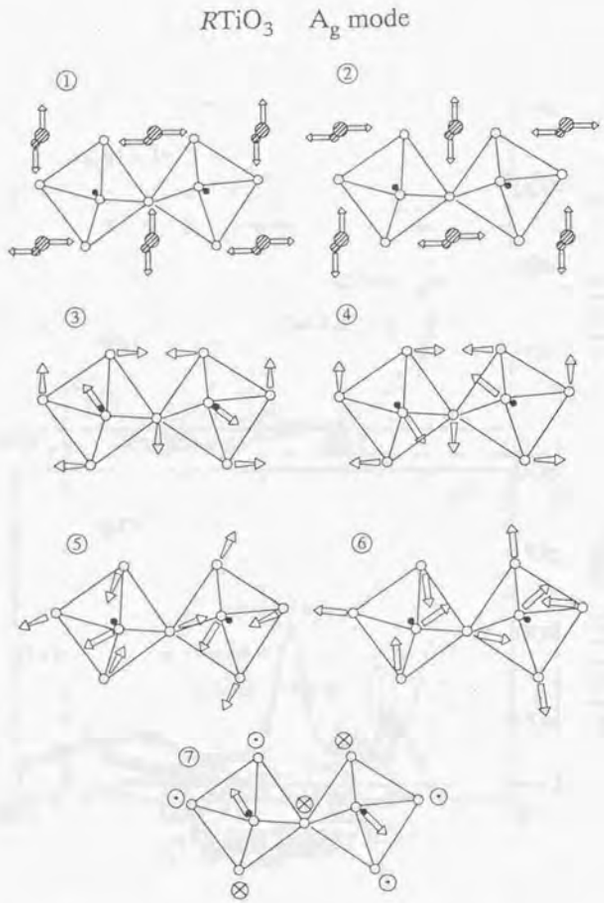

Figure 5.8: Normal coordinates of the A_{1g} modes from the calculation. Solid circles, open circles, and shaded circles represent Ti, O, and R atoms, respectively. Each number refers to the number in Fig. 5.7.

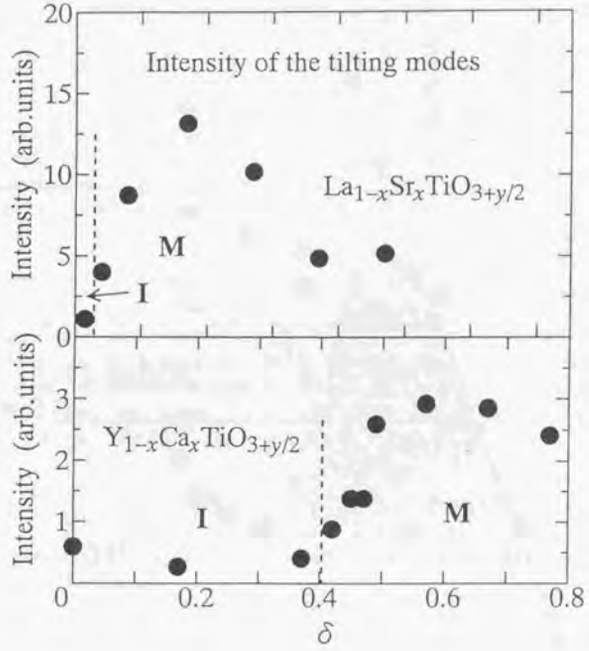

Figure 5.9: The phonon intensity of the tilting modes with the A_{1g} symmetry as a function of the hole concentration δ for R=La and Y. Dashed lines represent the metal-insulator phase boundary of each series.

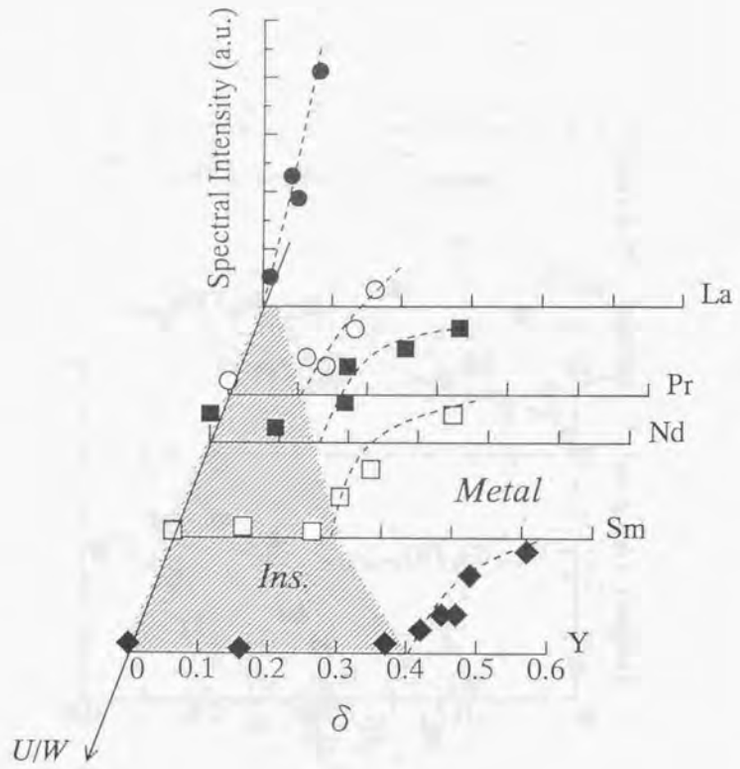

Figure 5.10: The phonon intensity of the tilting modes with the A_{1g} symmetry as a function of the hole concentration δ and the electron-correlation strength U/W. The shaded area represents the insulating region. Dashed lines are guide to the eyes.

to which the A_{1g} phonon belongs, is given by

$$\frac{d^2I}{d\Omega d\omega} \propto \frac{\gamma_{\rm ph}}{\gamma_{\rm ph}^2 + (\omega - \omega_{\rm ph})^2} |\delta\chi|^2, \tag{5.1}$$

where $\omega_{\rm ph}$ is the phonon frequency and γ_{ph} is the width of the phonon spectra. $\delta\chi$ is the modulation of the susceptibility by the atomic displacements, which is given by

$$\begin{aligned}\delta\chi &= -\frac{e^2}{m\omega_i^2 v} \sum_{\mathbf{H}} V^{(1)}(\mathbf{k}+\mathbf{H}) \\ &\times \sum_{\mathbf{k}_1}\sum_{\mathbf{k}_2} \frac{f(\mathbf{k}_1) - f(\mathbf{k}_2)}{E_{\mathbf{k}_1} - E_{\mathbf{k}_2}} \left(\mathbf{k}_1 \left| e^{-i\mathbf{k}\cdot\mathbf{r}} \right| \mathbf{k}_2\right) \left(\mathbf{k}_2 \left| e^{i(\mathbf{k}+\mathbf{H})\cdot\mathbf{r}} \right| \mathbf{k}_1\right),\end{aligned} \tag{5.2}$$

where ω_i is an incident light frequency, v a normalization volume, $\mathbf{k}$ the difference in wave numbers of an incident and scattered light, $\mathbf{H}$ a reciprocal lattice vector, $f(\mathbf{k}) = f(E_{\mathbf{k}})$ the Fermi distribution function, and $|\mathbf{k}\rangle$ the Bloch function. $V^{(1)}(\mathbf{k})$ is the Fourier coefficient of $V^{(1)}(\mathbf{r})$, which is the inner product of an atomic displacement and $\mathbf{r}$ derivative of the electron-ion potential. In the limit of $\mathbf{k} \ll \mathbf{k}_F$, $(\mathbf{k}_1|e^{-i\mathbf{k}\cdot\mathbf{r}}|\mathbf{k}_2)$ equals $\delta_{\mathbf{k}_2,\mathbf{k}_1+\mathbf{k}}$.

To elucidate the change of the phonon intensity with x in the metallic region of the titanium oxide system within the framework of the MMB theory, the most important term is $[f(\mathbf{k}_1) - f(\mathbf{k}_1+\mathbf{k})]/[E(\mathbf{k}_1) - E(\mathbf{k}_1+\mathbf{k})]$ in Eq. (5.2), whose $\mathbf{k}_1$ summation equals the response function. If we take account of the phonon frequency as an extension of the adiabatic MMB-theory, and neglect, as a crude approximation, the $\mathbf{k}$ and $\mathbf{k}_1$ dependence of $\sum_{\mathbf{H}} V^{(1)}(\mathbf{k}+\mathbf{H})(\mathbf{k}_1+\mathbf{k}|e^{i(\mathbf{k}+\mathbf{H})\cdot\mathbf{r}}|\mathbf{k}_1)$, then $\delta\chi$ becomes such as

$$\delta\chi \propto \sum_{\mathbf{k}_1} \frac{f(\mathbf{k}_1) - f(\mathbf{k}_1+\mathbf{k})}{E(\mathbf{k}_1) - E(\mathbf{k}_1+\mathbf{k}) + \hbar\omega_{\rm ph}} = \frac{k^2}{4\pi e^2} \left[\epsilon_\infty - \epsilon(\omega_{\rm ph}, \mathbf{k})\right], \tag{5.3}$$

where ϵ is the dielectric function. Accordingly, the intensity of the phonon spectrum in Raman scattering is given by

$$\frac{d^2I}{d\Omega d\omega} \propto \left| \frac{k^2}{4\pi e^2} \left[\epsilon_\infty - \epsilon(\omega_{\rm ph}, \mathbf{k})\right] \right|^2. \tag{5.4}$$

In the present experiment, the condition that $\omega_{\rm ph} > kv_F$ holds. Thus, we can approximate $\epsilon(\omega, \mathbf{k})$ by the Drude model;

$$\epsilon_\infty - \epsilon(\omega, \mathbf{k}) \sim \frac{4\pi n e^2}{m^*} \frac{1}{\omega^2 - i\Gamma\omega}, \tag{5.5}$$

where n is a carrier density, m^* an effective mass of the carriers, and Γ the inverse relaxation time of the carriers. In the low temperature limit, the origin of the relaxation

is the scattering by the impurity and here Γ may be regarded as nearly constant for the composition (x) range of interest. Then, Eqs. (5.4) and (5.5) indicate that the phonon intensity in the Raman-scattering spectra of metals is proportional to $(n/m^*)^2$.

To compare the experimental results with the MMB theory, we have plotted the *normalized* phonon intensity as a function of n/m^* in $La_{1-x}Sr_xTiO_{3+y/2}$ and $Y_{1-x}Ca_xTiO_{3+y/2}$ in Fig. 5.9. Here, we defined the normalized phonon intensity ($\tilde{I}$) as a division of the bare intensity by $\sin^2\theta$, where θ is a Ti-O-Ti bond angle, to correct the difference of orthorhombicity in each sample. [3] We derived n/m^* from electronic specific-heat coefficient (γ) [13, 17], which is proportional to $m^*n^{1/3}$, with the confirmed relation that the number of carrier per Ti site equals the band filling $1-x$. The scales of the ordinate and the abscissa are in arbitrary units, but the relative values for each sample can be compared with each other. As clearly seen in Fig. 5.11, the normalized intensity strongly correlates with n/m^*, and all the experimental points locate near the dashed line in Fig. 5.11 which represents the relation $\tilde{I} \propto (n/m^*)^2$.

The value of carrier effective mass (m^*) plays an important role in the MI transition of these titanate systems; i.e., m^* is critically enhanced as x is decreased to the MI phase boundary from the metallic side [13, 17, 16], owing to the electron correlation effect. Thus, the decrease of the phonon intensity in the metallic region when the system approaches the MI phase boundary (as shown in Fig. 5.9) is attributed to such enhancement of the carrier mass.

We should note that m^* appearing in Eq. (5.5) is a simple band mass, whereas the effective mass renormalized by the electron-correlation effect is used in the present discussion. In this sense, more sophisticated theory that takes account of the electron correlation effect directly would be desired. However, the MMB model with the assumption that m^* appearing in Eq. (5.5) corresponds to the effective mass renormalized by such a correlation effect seems to be quite a good standpoint, judging from the experimentally obtained relation $\tilde{I} \propto (n/m^*)^2$ in accordance with their theory.

5.6 Mode dependence of the Raman intensity

In Eq. (5.2), the phonon-mode-dependent term is only $V^{(1)}(\mathbf{k}+\mathbf{H})$, which represents the change of the electronic structure with the atomic displacement according to the normal

[3] The present phonon mode would not be Raman-active in the cubic perovskite, but becomes Raman-active because of the orthorhombic distortion. Therefore, variation of orthorhombicity also leads to variation of the phonon intensity. It is known that intensity of such a mode is proportional to the square of an order parameter of the distortion. [For example, see D. J. Lockwood *et al. Anharmonic Lattices, Structural Transitions and Melting* (Leiden, Noordhoff) 147 (1974); E. J. Samuelsen *et al.*, J. Phys. C **12**, 2007 (1979).] We here adopted $\sin\theta$ as the order parameter and corrected the effect of lattice distortion. The value of $\sin^2\theta$ is within the range of 0.082–0.216.

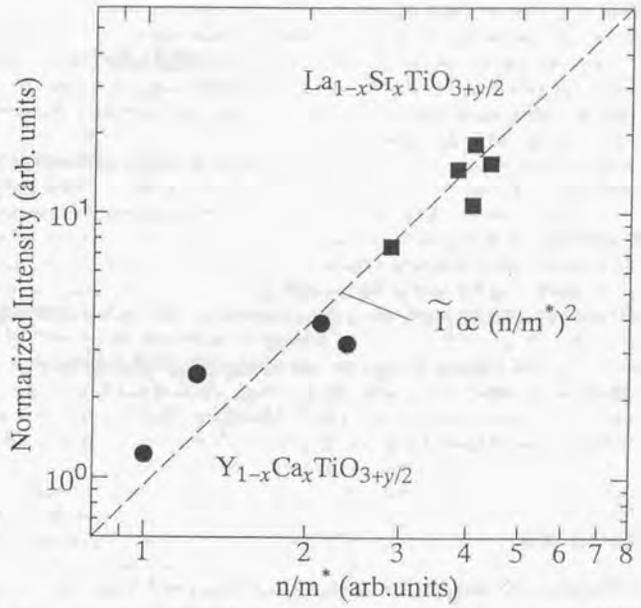

Figure 5.11: Normalized intensity of the A_{1g} tilting modes as a function of n/m^*; closed squares for $La_{1-x}Sr_xTiO_{3+y/2}$ and closed circles for $Y_{1-x}Ca_xTiO_{3+y/2}$. The magnitude of n/m^* is derived from the values of the electronic specific-heat coefficient. (See text.)

coordinate.

As described in the previous chapter, among the parameters of the crystal structure, the most dominant one for the electronic structure is the Ti-O-Ti bond angle, which determines the one-electron bandwidth of the conduction band. This Ti-O-Ti bond angle is determined by the tilting angle of TiO_6 octahedra. Thus, the tilting modes, which modulate the tilting angle of the TiO_6 octahedra, directly modulate the bandwidth of the conduction band of the metallic state. Thus, the term $V^{(1)}(\mathbf{k}+\mathbf{H})$ for the tilting modes is expected to be larger compared with that for other modes.

The reason why the rare-earth modes are also strong in their intensity is not clear so far. One possible interpretation is that the R/Ca(Sr) atom has a large effect on the electronic structure through the long-range Coulomb interaction (Mahdelung potential) and the displacement of the R/Ca(Sr) atom would modulate the charge distribution of the conduction band composed of Ti $3d$ and O $2p$ levels.

Such a strong spectral intensity of the specific phonon modes is observed in Raman scattering of several insulators. One example that should be compared with the present result is $LaMnO_3$,[67] where the Jahn-Teller distortion is prominent and is dominant for the electronic structure of the insulating phase. In the Raman spectrum of this compound, the "Jahn-Teller mode", which modulate the magnitude of the Jahn-Teller distortion (corresponding to the mode 5 and 6 in Fig. 5.8) is stronger in its intensity than other modes. This indicates that the electron-phonon coupling of the Jahn-Teller mode is stronger than that of other modes.

The present result of the titanates suggests that strong intensity of the specific phonon modes in the Raman spectrum of metals is also the consequence of a characteristic relation between the electronic structure and the lattice distortion. This implies that Raman-scattering can also be a good probe for the electronic structure and electron-lattice coupling of metals.

5.7 Summary

We measured Raman-scattering spectra for $R_{1-x}Ca_xTiO_{3+y/2}$ and found that the phonon spectra were observed only in the metallic region and their intensity decreases as the MI phase boundary is approached. These phonon Raman spectra are strongly coupled with the *intraband* excitation across the Fermi level, and their intensity bears close relation to the value of their carrier effective mass that is renormalized by the electron correlation effect. Among the Raman-allowed modes, the tilting modes in which the TiO_6 octahedra is rigidly tilting have strong intensity, which is consistent with the electronic structure of the present titanates that is strongly affected by the Ti-O-Ti bond angle.

Chapter 6

Conclusions

We have investigated the perovskite-type titanate $R_{1-x}Ca_xTiO_{3+y/2}$, whose bandwidth (or strength of electron correlation) and band filling can both be controlled by the change of the species of R (rare earth) and Ca doping/extra oxygen, respectively.

Charge-gap magnitude (E_g) of the end compound $RTiO_3$ as well as the hole concentration ($\delta = x + y$) required to make the sample metallic (δ_c) changes with the correlation strength in a way that $\propto U/W - (U/W)_c$, where $(U/W)_c$ is the hypothetical critical value of the bandwidth-control Mott transition for $n = 1$. The Néel temperature (T_N) in $RTiO_3$ decreases from La to Sm (with decreasing bandwidth W). T_N also decreases with hole doping, but remains finite as long as the compound remains insulating. An electronic phase diagram of $R_{1-x}Ca_xTiO_{3+y/2}$ as a typical electron-correlated system was obtained as a function of bandwidth and band filling.

The $R_{1-x}Ca_xTiO_{3+y/2}$ crystals on the verge of the phase boundary show characteristic behaviors, such as the transition from a high-temperature-metallic to a low-temperature-antiferromagnetic phase, and the transition from a high-temperature-paramagnetic-insulating to a low-temperature-metallic phase.

Optical spectra for $R_{1-x}Ca_xTiO_3$ were investigated, varying the strength of electron correlation (U/W) as well as the band filling $n = 1 - \delta$. With decrease of n from 1 (increase of δ from 0), the spectral weight of the Mott-gap excitation is reduced and that of the in-gap state increases linearly. The rate of the in-gap state evolution with δ is critically enhanced as U/W approaches $(U/W)_c$, in the manner of $[U/W - (U/W)_c]^{-1}$. It was also found that the metal-insulator transition at a finite hole doping level in a series of $R_{1-x}Ca_xTiO_{3+y/2}$ takes place when the spectral weight of the in-gap state in the optical conductivity reaches the common critical value.

Temperature dependence of optical spectra were investigated for $CeTiO_{3+y/2}$, which shows metallic conduction but antiferromagnetic ordering at 70 K, and $Ce_{0.95}Ca_{0.05}TiO_{3+y/2}$, which is a paramagnetic metal down to the lowest temperature. Extended Drude analysis has revealed that temperature dependence of the conductivity in the paramagnetic phase

can be attributed to the uniform change of the scattering rate of conduction carriers $1/\tau(\omega)$ against ω, whereas the effective mass $m^*(\omega)$ is almost T independent. Such a change of $1/\tau(\omega)$ with T is consistent with the Fermi-liquid theory, but in contrast to the behavior of the cuprate superconductors. On the other hand, optical conductivity of $CeTiO_{3+y/2}$ in the antiferromagnetic phase is decreased in the low-energy region with decreasing T, but does not show any gap-like structure even at the lowest temperature. Such a spectral change suggests that the spectral weight contributing the metallic conduction barely decrease with antiferromagnetic ordering, but the scattering rate $1/\tau(\omega)$ increases in the low-energy region.

We also measured Raman-scattering spectra for $R_{1-x}Ca_xTiO_{3+y/2}$ and found that the phonon spectra were observed only in the metallic region and their intensity decreases as the metal-insulator phase boundary is approached. These phonon Raman spectra are strongly coupled with the *intraband* excitation across the Fermi level, and their intensity bears close relation to the value of their carrier effective mass that is renormalized by the electron correlation effect. Among the Raman-allowed modes, the tilting modes in which the TiO_6 octahedra is rigidly tilting have strong intensity, which is consistent with the electronic structure of the present titanates that is strongly affected by the Ti-O-Ti bond angle.

In the present study, the physical properties of the electron-correlated system and their dependence on its bandwidth, band filling, and temperature have been clarified in quantitative ways. There are also several points that remain or newly appear as unresolved issues through this study:

1. The character of the antiferromagnetic metal near the MI phase boundary: How large is the spin moment and what is the wave vector of the antiferromagnetic ordering?

2. Is the transition from the antiferromagnetic insulator, through the antiferromagnetic metal, to the paramagnetic metal continuous with a change of band filling or bandwidth? If so, what is the critical exponent of such transitions ?

3. Is the change of optical spectra with temperature as observed in $Ce_{1-x}Ca_xTiO_{3+y/2}$ universal for other electron-correlated systems?

4. What is the origin of the insulating phase with finite hole doping? Is there any characteristic temperature dependence of, for example, optical spectra in this phase?

5. Are there any other systems that show similar phonon spectra and their effective-mass dependence as observed in Raman-scattering spectra of the titanates?

These issues will be clarified in future studies.

Chapter 7

Acknowledgement

I wish to express my gratitude to Prof. Y. Tokura for his guidance, suggestion, discussion, and encouragement in the course of this work. I am grateful to the following people for their collaboration in the experiment; Y. Taguchi, Y. Okada, Y. Fujishima, and T. Arima (sample preparation, transport and magnetic measurement), Y. Okimoto and T. Ishikawa (reflectivity measurement), and K. Yamamoto (Raman-scattering measurement). I am also grateful to Prof. A. Fujimori, Prof. M. Imada, and Prof. N. Nagaosa for useful discussions. I also thank all the members of Tokura Group for discussions and encouragement. Finally, I thank my wife Maki for her love and support.

The present work was supported by the fellowship from the Japan Society for the Promotion of Science, a Grant-in-Aid for Scientific Research from the Ministry of Education, Science, and Culture, Japan, and the New Energy and Industrial Technology Development Organization (NEDO) of Japan.

References

[1] N. F. Mott, *The Metal-Insulator Transition* (Taylor and Francis, London, 1974).

[2] D. B. MacWhan, A. Menth, J. P. Remeika, W. F. Brinkman, and T. M. Rice, Phys. Rev. B **7**, 1920 (1973), and references therein.

[3] For example, H. Takagi, T. Ido, S. Ishibashi, M. Uota, S. Uchida, and Y. Tokura, Phys. Rev. B **40**, 2254 (1989).

[4] M. Imada, J. Phs. Soc. Jpn. **64**, 2954 (1995).

[5] M. A. Continentino, Phys. Rep. **239**, 178 (1994).

[6] D. A. MacLean, Hok-Nam Ng, and J. E. Greedan, J. Solid State Chem. **30**, 35 (1979).

[7] D. A. MacLean, K. Seto, and J. E. Greedan, J. Solid State Chem. **40**, 241 (1981).

[8] J. E. Greedan, J. Mag. Mag. Mat. **44**, 299 (1984).

[9] J. E. Greedan, J. Less-Common Met. **111**, 335 (1985).

[10] F. Lichtenberg, D. Widmer, J. G. Bednorz, T. Williams, and A. Reller, Z. Phys. B **84**, 369 (1991).

[11] Y. Fujishima, Y. Tokura, T. Arima and S. Uchida, Phys. Rev. **B46**, 11167 (1992).

[12] D. A. Crandles, T. Timusk, J. D. Garett, and J. E. Greedan, Physica C **201**, 407 (1992)

[13] Y. Tokura, Y. Taguchi, Y. Okada, Y. Fujishima, T. Arima, K. Kumagai, and Y. Iye, Phys. Rev. Lett. **70**, 2126 (1993).

[14] Y. Taguchi, Y. Tokura, T. Arima, and F. Inaba, Phys. Rev. B **48**, 511 (1993).

[15] Y. Okada, T. Arima, Y. Tokura, C. Murayama, and N. Mori, Phys. Rev. B **48**, 9677 (1993).

[16] Y. Tokura, Y. Taguchi, Y. Moritomo, K. Kumagai, T. Suzuki, and Y. Iye, Phys. Rev. B **48**, 14 063 (1993).

[17] K. Kumagai, T. Suzuki, Y. Taguchi, Y. Okada, Y. Fujishima, and Y. Tokura, Phys. Rev. B **48**, 7636 (1993).

[18] Y. Tokura and T. Katsufuji, in *Spectroscopy of Mott Insulators and Correlated Metals* edited by A. Fujimori and Y. Tokura (Springer).

[19] H. L. Ju, C. Eylem, J. L. Peng, B. W. Eichhorn, and R. L. Greene, Phys. Rev. B **49**, 13 335 (1994).

[20] G. Amow and J. E. Greedan, J. Solid State Chem. **121**, 443 (1996).

[21] M. J. Rozenberg, G. Kotliar, and X. Y. Zhang, Phys. Rev. B **49**, 10181 (1994)

[22] W. A. Harrison, Electronic Structure and Properties of Solids (Freeman, San Francisco, 1980).

[23] M. J. Rozenberg, X. Y. Zhang, and G. Kotliar, Phys. Rev. Lett. **69**, 1236 (1992)

[24] A. Georges and W. Krauth, Phys. Rev. Lett. **69**, 1240 (1992).

[25] J. P. Goral, J. E. Greedan, and D. A. MacLean, J. Solid State Chem. **43**, 244 (1982).

[26] T. Mizokawa and A. Fujimori, Phys. Rev. B **54**, 5368 (1996).

[27] J. Akimitsu, private communication.

[28] H. Sawada, N. Hamada, and K. Terakura, Physica B **237-238**, 46 (1997).

[29] G. M. Luke, B. J. Sternlieb, Y. J. Uemura, J. H. Brewer, R. Kadno, R. F. Kiefl, S. R. Kreitzman, T. M. Riseman, J. Gopalakrishman, A. W. Sleight, M. A. Subramanian, S. Uchida, H. Takagi, and Y. Tokura, Nature (London) **338**, 49 (1989).

[30] F. Inaba, T. Arima, T. Ishikawa, T. Katsufuji, and Y. Tokura, Phys. Rev. B **52**, R2221 (1995).

[31] S. A. Carter, T. F. Rosenbaum, J. M. Honig, and J. Spalek, Phys. Rev. Lett. **67**, 3440 (1991).

[32] W. Bao, C. Broholm, S. A. Carter, T. F. Rosenbaum, G. Aeppli, S. F. Trevino, P. Metcalf, J. M. Honig, and J. Spalek, Phys. Rev. Lett. **71**, 766 (1993).

[33] J. A. Wilson, *The Metallic and Nonmetallic State of Matter*, edited by P. P. Edwards and C. N. R. Rao (Taylor and Francis, London, 1985), p.215-261.

[34] S. Miyasaka, H. Takagi, Y. Sekine, H. Takahashi, and N. Môri, unpublished.

[35] Th. Pruschke, D. L. Cox, and M. Jarrell, Phys. Rev. B **47**, 3553 (1993).

[36] S. Uchida, T. Ido, H. Takagi, T. Arima, Y. Tokura, S. Tajima, Phys. Rev. B **43**, 7942 (1991).

[37] S. L. Cooper, G. A. Thomas, J. Orenstein, D. H. Rapkine, A. J. Millis, S.-W Cheong, A. S. Cooper, and Z. Fisk, Phys. Rev. B **41**, 11 605 (1990).

[38] T. Arima, Y. Tokura, and S. Uchida, Phys. Rev. B **48** 6597 (1993).

[39] For example, L. D. Rotter *et al.*, Phys. Rev. Lett. **67**, 2741 (1991), and references therein.

[40] A. V. Puchkov, P. Fournier, D. N. Basov, T. Timusk, A. Kapitulnik, and N. N. Kolesnikov, Phys. Rev. Lett. **77**, 3212 (1996).

[41] D. N. Basov, R. Liang, B. Dabrowski, D. A. Bonn, W. N. Hardy, and T. Timusk, Phys. Rev. Lett. **77**, 4090 (1996).

[42] G. A. Thomas, D. H. Rapkine, S. A. Carter, A. J. Millis, T. F. Rosenbaum, P. Metcalf, and J. M. Honig, Phys. Rev. Lett. **73**, 1529 (1994).

[43] M. Kasuya, Y. Tokura, T. Arima, H. Eisaki, and S. Uchida, Phys. Rev. B **47**, 6197 (1993).

[44] E. Dagotto, A. Moreo, F. Ortolani, D. Poilblanc, and J. Riera, Phys. Rev. B **45**, 10 741 (1992).

[45] H. Eskes and A. M. Oleś, Phys. Rev. Lett. **73**, 1279 (1994).

[46] M. Ogata and H. Shiba, Phys. Rev. B **41**, 2326 (1990).

[47] A. J. Millis and S. N. Coppersmith, Phys. Rev. B **42**, 10 807 (1990).

[48] A. Urushibara, Y. Moritomo, T. Arima, A. Asamitsu G. Kido, and Y. Tokura, Phys. Rev. B **51**, 14 103 (1995).

[49] A. J. Millis, R. Mueller, and B. I. Shraiman, Phys. Rev. B **54**, 5389 (1996).

[50] N. W. Ashcroft and N. D. Mermin, *Solid State Physics* (Saunders College, Philadelphia, 1976).

[51] J. W. Allen and J. C. Mikkelsen, Phys. Rev. B **15**, 2952 (1977).

[52] D. Pines and P. Nozieres, *The Theory of Quantum Liquids* (Benjamin, New York. 1966).

[53] D. A. Bonn, J. D. Garrett, and T. Timusk, Phys. Rev. Lett. **61**, 1305 (1988).

[54] T. Katsufuji, M. Kasai, and Y. Tokura, Phys. Rev. Lett. **76**, 126-129 (1996).

[55] C. Herring, in *Magnetism*, edited by G. T. Rado and H. Suhl (Academic Press, New York, 1967).

[56] A. W. Overhauser, Phys. Rev. **128**, 1437 (1962).

[57] A. S. Barker, Jr., B. I. Halperin, and T. M. Rice, Phys. Rev. Lett. **20**, 384 (1968).

[58] L. Degiorgi, M. Dressel, A. Schwartz, B. Alavi, and G. Grüner, Phys. Rev. Lett. **76**, 3838 (1996).

[59] Y. Taguchi and Y. Tokura, unpublished.

[60] L. F. Mattheiss, Phys. Rev. B **6**, 4718 (1972); *ibid*, Phys. Rev. **181**, 987 (1969).

[61] Y. Okada, Y. Taguchi, Y. Tokura, and Y. Iye, unpublished.

[62] Cardona, *Light Scattering in Solids I*, (Springer, Berlin, 1983).

[63] T. Katsufuji and Y. Tokura, Phys. Rev. B **49**, 4372 (1994).

[64] M. Couzi and P. Vam Huong, J. Chim. Phys. **69**, 1339 (1972).

[65] J. E. Sunstrom IV, S. M. Kauzlarich, and P. Klavins, Chem. Mater. **4**, 346 (1992).

[66] D. L. Mills, A. A. Maradudin, and E. Burstein, Annals of Physics **56**, 504 (1970).

[67] K. Yamamoto, T. Katsufuji, A. Urushibara, Y. Moritomo, and Y. Tokura, unpublished.

PUBLICATION LIST

1. T. Katsufuji, Y. Taguchi, and Y. Tokura,
"Transport and magnetic properties of a Mott-Hubbard system whose bandwidth and band-filling are both controllable: $R_{1-x}Ca_xTiO_{3+y/2}$
Phys. Rev. B, in press.

2. K. Yamamoto, T. Katsufuji, T. Tanabe, Y. Tokura,
"Raman scattering of the charge-sin stripes in $La_{1.67}Sr_{0.33}NiO_4$"
submitted to Phys. Rev. Lett.

3. T. Katsufuji, T. Tanabe, T. Ishikawa, Y. Fukuda, T. Arima, and Y. Tokura,
"Optical spectroscopy of the charge-ordering transition in $La_{1.67}Sr_{0.33}NiO_4$"
Phys. Rev. B **54**, R14230-R14233 (1997).

4. Y. Okimoto, T. Katsufuji, T. Ishikawa, T. Arima, and Y. Tokura,
"Variation of electronic structure in $La_{1-x}Sr_xMnO_3$ ($0 \leq x \leq 0.3$) as investigated by optical conductivity spectra"
Phys. Rev. B **55**, 4206-4214 (1997).

5. T. Katsufuji, M. Kasai, and Y. Tokura,
"In-plane and out-of-plane optical spectra of Sr_2RuO_4"
Phys. Rev. Lett. **76**, 126-129 (1996).

6. T. Katsufuji, Y. Okimoto, and Y. Tokura,
"Spectral weight transfer of the optical conductivity in doped Mott insulators"
Phys. Rev. Lett. **75**, 3497-3500 (1995).

7. F. Inaba, T. Arima, T. Ishikawa, T. Katsufuji, and Y. Tokura,
"Change of electronic properties on the doping-induced insulator-metal transition in $La_{1-x}Sr_xVO_3$"
Phys. Rev. B **52**, R2221-R2224 (1995).

8. Y. Okimoto, T. Katsufuji, T. Ishikawa, A. Urushibara, T. Arima, and Y. Tokura,
"Anomalous variation of optical spectra with spin polarization in double-exchange ferromagnet: $La_{1-x}Sr_xMnO_3$"
Phys. Rev. Lett. **75**, 109-112 (1995).

9. Y. Tokura and T. Katsufuji
"Optical spectroscopy on the Mott transition in perovskite-type titanates"
in *Spectroscopy of Mott Insulators and Correlated Metals* edited by A. Fujimori and Y. Tokura (Springer).

10. Y. Okimoto, T. Katsufuji, Y. Okada, T. Arima, and Y. Tokura,
"Optical spectra in $(La,Y)TiO_3$: Variation of Mott-Hubbard gap features with change of electron correlation and band filling"
Phys. Rev. B **51**, 9581-9588 (1995).

11. T. Katsufuji, Y. Okimoto, T. Arima, Y. Tokura, and J. B. Torrance,
"Optical spectroscopy of the metal-insulator transition in $NdNiO_3$"
Phys. Rev. B **51**, 4830-4835 (1995).

12. T. Katsufuji and Y. Tokura,
"Electronic Raman scattering spectra in strongly correlated metals: cuprate superconductors and titanium oxide"
Physica C **235-240**, 1147-1148 (1994).

13. T. Katsufuji and Y. Tokura,
"Anomalous variation of phonon Raman intensities near the metal-to-Mott-insulator transition in titanium oxide system"
Phys. Rev. B **50**, 2704-2707 (1994).

14. T. Katsufuji and Y. Tokura,
"Electronic Raman scattering in filling-controlled metals: $Sr_{1-x}La_xTiO_3$"
Phys. Rev. B **49**, 4372-4375 (1994).

15. T. Katsufuji, Y. Tokura, T. Ido, and S. Uchida,
"Symmetry-dependent electronic Raman scattering in $La_{2-x}Sr_xCuO_4$: Evidence for doping-induced change in k-space anisotropy of charge dynamics"
Phys. Rev. B **48**, 16131-16134 (1993).

16. Y. Tokura, Y. Taguchi, Y. Okada, T. Katsufuji, T. Arima, and K. Kumagai,
"Change of electronic structures with hole doping in strongly correlated electron systems: titanium oxides"
Physica B **186-188**, 992-994 (1993).

17. Y. Moritomo, T. Katsufuji, and Y. Tokura,
"Dielectric phase transition and symmetry change of constituent molecules in proton-deuteron mixed crystals of squaric acid"
J. Chem. Phys. **95**, 2244-2251 (1991).